Dyke-induced graben formation in a heterogeneous succession on Mt Etna: Insights from field observations and FEM numerical models

Kyriaki Drymoni[1*], Elena Russo[1,2], Alessandro Tibaldi[1,2], Noemi Corti[1], Fabio Luca Bonali[1,2], Federico Pasquarè Mariotto[3]

[1]Department of Earth and Environmental Sciences, University of Milan-Bicocca, 20126 Milan, Italy
[2]CRUST-Interuniversity Center for 3D Seismotectonics with Territorial Applications, 66100 Chieti Scalo, Italy
[3]Department of Human and Innovation Sciences, Insubria University, Como, Italy

Abstract

The most common way of magma transfer toward the surface is through dyking. Dykes can generate stresses at their tips and the surrounding host rock, initiating surficial deformation, seismic activity, and graben formation. Although scientists can study active deformation and seismicity via volcano monitoring, the conditions under which dykes induce grabens during their emplacement in the shallow crust are still enigmatic. Here, we explore through FEM numerical modelling the conditions that could have been associated with dyke-induced graben formation during the 1928 fissure eruption on Mt Etna (Italy). We use stratigraphic data of the shallow host rock successions along the western and eastern sections of the fissure that became the basis for several suites of numerical models and sensitivity tests. The layers had dissimilar mechanical properties, which allowed us to investigate the studied processes more realistically. We investigated the boundary conditions using a dyke overpressure range of 1-10 MPa and a local extensional stress field of 0.5-2 MPa. We studied the effect of field-related geometrical parameters by employing a layer thickness range of 0.1-55 m and a variable layer sequence at the existing stratigraphy. We also tested how more compliant pyroclastics, such as scoria, (if present) could have affected the accumulation of stresses around the dyke. Also, we explored how inclined sheets and vertical dykes can generate grabens at the surface. We propose that the mechanical heterogeneity of the flank

succession and the local extensional stress field can largely control ~~both~~ the dyke path and dyke-induced graben formation regardless of increased dyke overpressure values. Similarly, soft materials in the stratigraphy can greatly suppress the shear stresses in the vicinity of a propagating dyke, encouraging narrow grabens at the surface if only the fracturing condition is satisfied, while inclined sheets tend to form semigrabens, respectively. Finally, we provide some insights related to the structural evolution of the 1928 lateral dyking event. All the latter can be theoretically applied in similar case studies worldwide.

Keywords: graben, Etna, FEM numerical modelling, fault, dyke arrest, inclined sheet

1. Introduction

Dykes are Mode I extension fractures that transfer magma to the surface driven almost entirely by the magma overpressure (Rubin and Pollard, 1988; Delaney et al., 1986, 1998; Gudmundsson, 2011; Tibaldi, 2015; Acocella, 2021). The propagation of a dyke is mechanically controlled by the local stress field. It occurs almost entirely perpendicular to the minimum principal compressive stress or tensile stress of the fracture (σ_3) although case studies exist where different conditions are met (Rubin and Polard, 1987; Segall et al., 2001; Hooper et al., 2011; Heimisson et al., 2015). Still, if a dyke is deflected into an active fault, it advances perpendicularly to the normal stress (σ_n) (Gudmundsson, 2011). During their ascent, dykes change their paths following the most economical trajectories (Gudmundsson, 1984, 2020, 2022; Rivalta et al., 2019) and basically, following the principle of least energy or least resistance (Gudmundsson, 1984, 2022; Dahm, 2000; Maccaferri et al., 2011; Reddy, 2013). As a result, they occasionally become arrested at mechanical discontinuities (Drymoni et al., 2020) or deflected into pre-existing fractures such as faults, other dykes or joints (Browning and Gudmundsson, 2015; Ruz et al., 2020; Clunes et al., 2021; Drymoni et al., 2021). However, dykes make their own paths most of the time, and if the conditions of mechanical arrest are not met, they feed volcanic eruptions (Gudmundsson, 2011).

As a dyke rises, it breaks the host rock and induces differential stress that produces seismicity mostly at its propagating tips and surrounding host rock (e.g. Dieterich and Decker, 1975; Broek, 1982; Pollard et al., 1983; Rubin and Pollard, 1988; Rubin, 1992, 1993; Dahm, 2000; Roman and Cashman, 2006; Roman et al., 2006; Grandin et al., 2011; Abdelmalak et al., 2012; Passarelli et al., 2012; Ágústsdóttir et al., 2016; Koehn et al., 2019; Gudmundsson, 2020, 2022) as well as deformation such as faulting, and extensional fracturing at the surface (e.g. Mastin and Pollard, 1988; Chadwick and Embley, 1998; Gudmundsson, 2003; Rowland et al., 2007; Biggs et al., 2009; Ebinger et al., 2010; Holland et al., 2011; Trippanera et al., 2014, 2019; Acocella and Trippanera, 2016; Ruch et al., 2016; Xu et al., 2016; Tibaldi et al., 2022). Consequently, propagating dykes can either reactivate pre-existing faults (Gudmundsson, 1984; Maccaferri et al., 2016) or generate new ones by forming grabens at the surface (Mastin and Pollard, 1988; Al Shehri and Gudmundsson, 2018; Bazargan and Gudmundsson, 2019). The latter can also alter the topography (Carbotte et al., 2006; Buck et al., 2006; Ruch et al., 2016), control the geometry and propagation of faults (Manighetti et al., 2004; Dumont et al., 2017) and also affect the propagation of the dyke that triggered the event itself (Mériaux and Lister, 2002; Rivalta and Dahm, 2004). Therefore, although analogue, analytical and numerical models, as mentioned above, have explored dyke-induced graben development, the mechanical and geometrical conditions that can potentially provoke or discourage the formation of a graben from a dyking event are still unclear.

The 1928 fissure eruption of Mt Etna (Italy) is a field example of a dyke-induced graben event (Branca et al., 2017). The structural data derived from it have provided valuable insights into the relationship between dyking and faulting (Tibaldi et al., 2022). The episode, which destroyed the town of Mascali, started in November 1928 and resulted in the opening of three WSW-ENE-aligned eruptive fissures. According to the timing of their formation, the fissures demonstrate a dyke-induced eastward propagation (Branca et al., 2017). Dyke-induced structures that can be observed in the area range from symmetric to half-grabens, from dry to eruptive fissures and finally, volcanic vents, making it an ideal case study for joint structural and FEM (Finite Element Method) numerical modelling analyses.

This work is a compound numerical study of the Tibaldi et al. (2022) volcanotectonic survey. Here, we jointly use the structural data collected by Tibaldi et al. (2022) in conjunction with the stratigraphic interpretations of Branca et al., (2011a), as input data to FEM numerical models. The primary aim is to explore the geometrical and mechanical conditions that could have been associated with the dyke-induced graben formation process during the 1928 fissure eruption event of Mt Etna. Specifically, we use two sets of stratigraphic data that expand on the western and eastern part of the fissure, respectively, to realistically assess the lateral propagation of the dyke that formed the dyke-induced grabens. In the first part, we attempt to gain insights into the dyking scenarios (propagation/arrest) based on the heterogeneous crustal segments of the studied sites. Then, we explore the mechanical conditions that could have triggered the dyke-induced grabens. In the second part of the numerical study, we use the eastern stratigraphic sequence to design suites of sensitivity tests and investigate how changes in the local stratigraphy and dyke geometry such as the dyke dip, the sequence of the layers, the thickness of the layers and combinations of those parameters can encourage graben formation in similar volcanotectonic settings. Finally, our work enables gaining insights into the following issues: i) Which parameters could have generated stress barriers and changed the path of the 1928 fissure eruption? ii) Which parameters possibly affected the tensile and shear stress concentration at the dyke tip and encouraged the formation of a graben or a semigraben during the lateral propagation of the 1928 fissure? iii) What was the mechanical and geological evolution of the 1928 fissure while the latter was propagating vertically but also laterally? Our models provide a robust field-numerical methodology that can be applied to different geotectonic settings.

2. Geological background

2.1 Regional settings

Mt. Etna, eastern Sicily, is one of the most active volcanoes on Earth, consisting of a large basaltic composite stratovolcano formed during the last 500 ka. Its geological evolution is divided into four main evolutionary phases of eruptive activity: the Basal Tholeiitic (500-330 ka), Timpe (220-110 ka), Valle del Bove (110-60 ka) and Stratovolcano (60 ka-Present) phases (Branca et al., 2011a, b). These phases are separated either by erosive periods or volcanotectonic events, such as the development of a summit caldera or its lateral failure, which produced an amphitheatre depression, open to the east, known as “Valle del Bove”.

Mt Etna is located in a compressional setting at the border between the African and European plates (Fig. 1a) (Lanzafame et al., 1997; Cocina et al., 1997, 1998). Regional compression is expressed by a horizontal N-S to NNW-SSE maximum principal stress (σ_1) vector that produces fault slip along WSW-ENE reverse faults and NW-SE strike-slip faults (Villani et al., 2020). Towards the east, offshore suites of transtensional and reverse faults exist, linked to the interaction with the Ionian microplate (Gambino et al., 2022).

This regional stress field is replaced within Mt Etna by a more locally active stress field related to magmatic and gravity forces. Due, in particular, to gravity effects, the whole eastern flank of the volcano is subject to an E-W to WNW-ESE horizontal σ_3 local stress field. The eastward lateral instability of the area produces sliding of the cone flank towards the sea and several faults that affect the northeast, east and southeast sectors of the volcano (Fig. 1b) (Kieffer, 1985; Neri et al., 1991; Borgia et al., 1992; McGuire and Saunders, 1993). The sliding occurs at rates of 2 cm/yr and even higher during periods of flank slip acceleration (Groppelli and Tibaldi, 1999; Tibaldi and Groppelli, 2002; Palano et al., 2009) and this motion of the eastern flank is accompanied by active faulting along its margins and complex internal deformation.

Focusing on our research area, the previous geotectonic interactions led to the development of the ENE Rift (Fig. 1b) (McGuire and Pullen, 1989; Azzaro et al., 2012; Cappello et al., 2012) where the 1928 fissure eruption occurred. The latter is composed of a swarm of ENE-striking normal faults, dry and eruptive fissures and aligned pyroclastic cones, described more in detail in the following chapter.

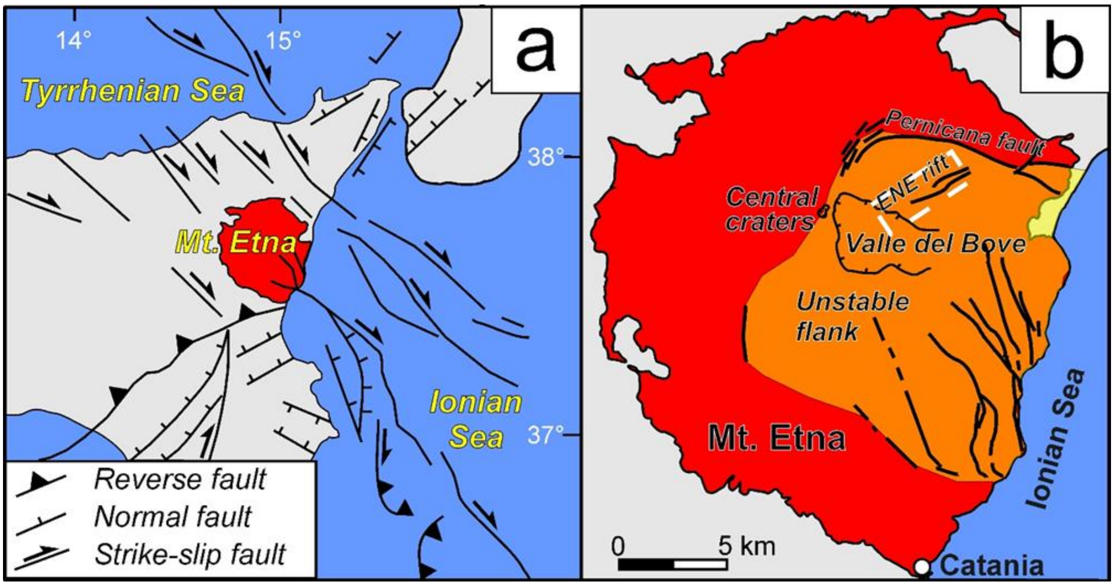

Figure 1. *(a) Geological map showing the geodynamic setting of Mt Etna, (b) main structures of Mt Etna; the white dashed box marks the location of the studied eruptive fissure (a and b are modified after Villani et al., 2020 and Gambino et al., 2022 for the offshore faults) as shown in Fig.2.*

2.2 The ENE Rift and 1928 Fissure

The study area includes a segment of the ENE rift (Fig. 1b), one of the main weakness zones of Mt Etna, which represents an ideal path for magma ascent. This area gives rise to flank eruptions, which are usually fed by shallow (1–3 km) dykes propagating laterally from the central conduit (Acocella and Neri, 2009).

The shallowest volcanic succession in the area belongs to the Mongibello Volcano (last 15 ka), which follows the older Ellittico Volcano (60 - 15 ka) (Branca et al., 2011a, b). The Mongibello sequence consists of basaltic lava flows, generated by central and flank eruptions, interlayered with pyroclastic fall deposits and breccias. The 1928 lateral eruption formed an ENE-WSW-trending system of 7.7-km-long, dry and eruptive fissures and faults (Branca et al., 2011b; Tibaldi et al., 2022).

The 1928 fissure swarm is of great geological-structural importance, as it consists of four settings with different deformation styles that are associated with dyke propagation processes: i) a sequence of eight eruptive vents in the uppermost part (about 2050 - 2350 m a.s.l.), ii) a 2.5-km-long single eruptive fissure in the intermediate part (about 1600 – 2050 m a.s.l.), iii) an area of dry and extension fractures, normal faults and a graben structure (about 1500 - 1600 m a.s.l.), and iv) an alignment of vents along the pre-existing Ripe della Naca fault system (about 1170 - 1230 m a.s.l.) (Tibaldi et al., 2022) (Fig. 2a).

Field structural data (Groppelli and Tibaldi, 1999; Tibaldi and Groppelli, 2002) and GPS data (Palano et al., 2009) indicate that the seaward motions along the northern border (Pernicana Fault, Fig. 1b) of the unstable volcano flank, which lies close to the easternmost section of the 1928 fissure, is in the order of 2 cm/yr. Towards the western section of the 1928 fissure, the eastward flank motion tends to decrease, as indicated by GPS data of different periods (Bonforte et al., 2007; Palano et al., 2009; Palano, 2016). These critical observations have been used to quantify the range of extension used in the numerical models, as described in detail below.

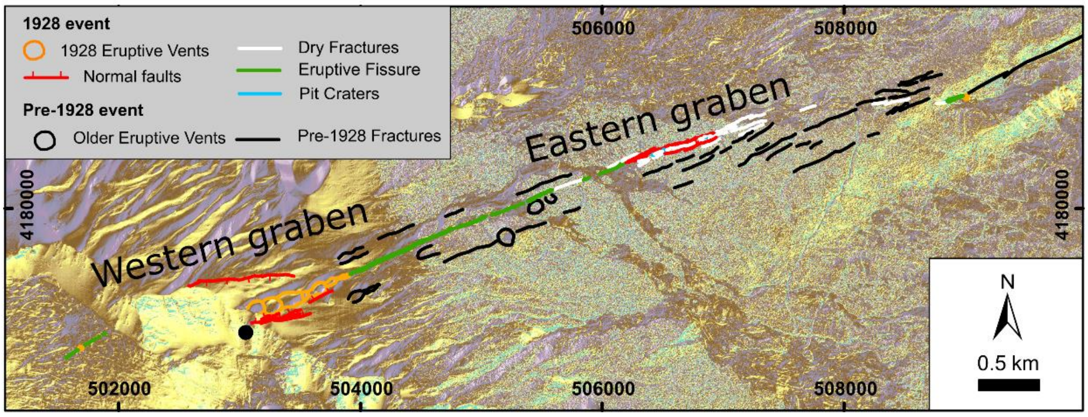

Figure 2. *The location of the 1928 fissure showing the field structures. Reference System: WGS 84-UTM 33N (modified from Tibaldi et al., 2022). The black dot represents the location of the stratigraphic column detailed in Fig. 3*

3. Input data and methods

3.1 Field Data

Tibaldi et al. (2022) reconstructed the geometry and kinematics of the extension fractures and normal faults resulting from the ENE propagation of the 1928 related dyke. In the present study, we focus on two sites that lie: i) in the western part (Fig. 2b) and ii) in the eastern part (Fig. 2c) of the fissure, respectively. In the first one, the dyke generated a graben accompanied by an eruption. This is testified to the fact that, in the middle of the graben, there is a series of ENE-elongated and aligned craters emplaced in 1928 (Branca et al., 2011b). In the second case, the fracture propagated shallower, inducing a semigraben that laterally passes to a graben; it is worth noting that here the dyke did not reach the surface. Further geological details about the two studied sites are provided below.

Western site

The western site (Fig. 2b) is characterised by eight eruptive vents, with an ENE-WSW alignment, surrounded by a 385-m-wide graben. This graben keeps the same width moving to the ENE with a decreasing elevation from 2590 to 2220 m a.s.l. for the northern fault and from 2300 to 2160 m a.s.l. for the southern fault, respectively. Moving further towards ENE, from 2160 to 2100 m a.s.l., there is only a minor fault with a 0.5-m offset, close to the 1928 eruptive vents. Beyond that, no normal faults are visible at lower elevations.

The architecture of the western dyke-induced graben is made up of normal faults striking E-W to ENE-WSW (Figs. 2b). Only one major fault is present along the northern side of the graben, with normal offsets ranging from 1 to 3 m. On the contrary, along the southern side of the graben, one main fault with vertical offset up to 10 m can be found. The latter is accompanied by minor, shorter faults with an offset in the order of 0.5 m.

Along the northern escarpment of the Valle del Bove, in correspondence with the 1928 eruptive vents, we report the location of a known stratigraphic log (Branca et al., 2011a) (Fig. 2a). The stratigraphic column (Fig. 3) comprises two main formations, subdivided into a series of volcanic units (A-L) with different characteristics. From bottom to top, we observe the Serra delle Concazze sequence, which dips 15-20° towards the NE and is composed of volcanic products of the Ellittico volcano (60-15 ka, Branca et al., 2011a), as seen below:

A) Porphyritic lava flows. Thickness = 10 m;

B) Thick sequence of brecciated layers, crossed by the 1971 and the 1986/87 eruptive fissures. Thickness = 40 m;

C) Subaphyric lava flows. Thickness = 55 m;

D) Scoriaceous breccia deposits. Thickness = 20 m;

E) Compact subaphyric lava flows. Thickness = 5 m;

F) Scoriaceous breccia deposits. Thickness = 19 m;

G) Sequence of lavas and breccias. Thickness = 6 m;

H) Sequence of thin lava flows intercalated with scoriae deposits. Thickness = 5 m;

I) Sequence of epiclastic and scoriaceous breccia deposits with lava units. Thickness = 40 m.

Due to local-scale erosional processes, an angular unconformity separates the Serra delle Concazze sequence from the above Pietracannone deposit (Branca et al., 2011a). The latter is related to the Mongibello volcano (last 15 ka, Branca et al., 2011a), and is composed of the L unit, which corresponds to 30-m thick lava flows (Fig. 3).

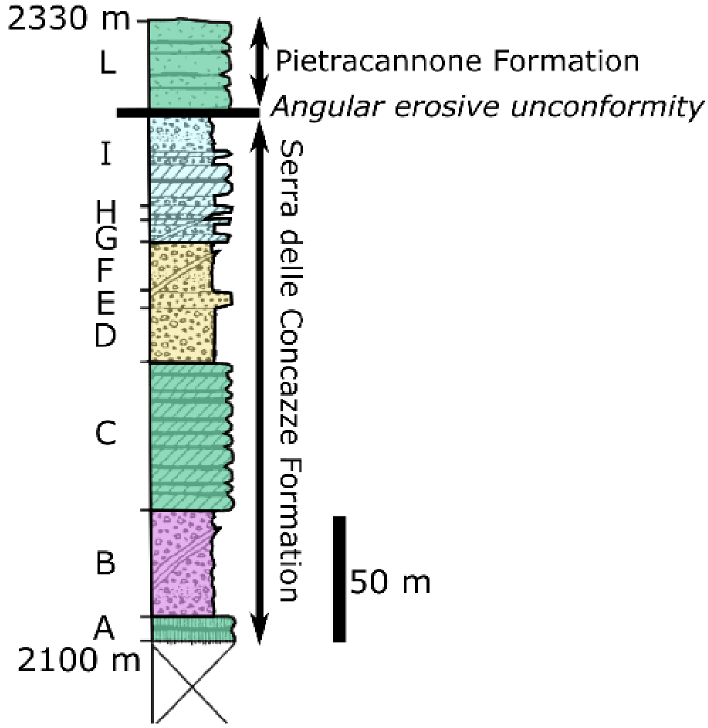

Figure 3. Detailed stratigraphic column of the western site, located along the northern escarpment of the Valle del Bove area (exact location shown in Fig. 2). Units A-I represent subunits of the Serra delle Concazze formation of the Ellittico Volcano (60 – 15 ka). Unit L belongs to the Pietracannone formation of the Mongibello Volcano (last 15 ka) (modified from Branca et al., 2011a).

Eastern site

Moving from the west to the east, our eastern site (Fig. 2) is composed of a half-graben followed by a symmetric graben, with widths of 74 m and 68 m, respectively. However, from the north to the south the faults show some dissimilarities. In specific, the northern half-graben side is formed by SE-dipping normal faults, with offsets ranging from 0.3 to 1.2 m. In contrast, the southern side is characterised by dry extension fractures without any evidence of vertical offset.

Similarly, the symmetric graben has NNW-dipping and SSE-dipping faults with a range of vertical offsets between 0.3 m and 3.5 m, with a maximum value measured along the northern graben side. Furthermore, extension fractures show, on average, a minor right-lateral component of motion. Tibaldi et al. (2022) have detected extension fractures in its central part with average aperture values less than 1 m and a maximum of 2.7 m.

Finally, based on the field observations from the same study, a typical shallow stratigraphic sequence is composed of two lava units intercalated with a tuff deposit.

The thickness of the lavas is 1 m for the bottom layer and 0.2 m for the top layer. The thickness of the intermediate tuff layer is also 1 m.

3.2 Numerical modelling method

3.2.1 Material properties

The shallow crust where the 1928 fissure eruption occurred, as shown by previous field studies (Branca et al., 2011a; Tibaldi et al., 2022), is highly heterogeneous. In this study, we used realistic values (cf. Gudmundsson, 2011; Heap et al., 2020) for the stiffness of the seven dissimilar layers based on in situ measurements (Bell, 2000), since laboratory values are usually greater (Gudmundsson, 2011).

The host rock material represents the bottom layer of the stratigraphic columns (Fig. 4). In numerical applications, the latter usually takes values between 10-40 GPa (Gudmundsson, 2020) or 1-15 GPa for shallow segments (Becerril et al., 2013). In our models, we tested a range of host rock values of 5-40 GPa. The tests have shown that this range did not alter the trajectories of σ_1 hence the host rock stiffness could not affect the dyke path. In addition to the above, as the stratigraphic analyses introduced many lava layers, we used a constant host rock value of 30 GPa in all the models to allow the software to recognise the basement deposits. For stiff materials such as lavas and lavas with breccia intercalations, we used values of 10 GPa and 7 GPa. For compliant (soft) materials such as tuffs, basaltic breccia with minor lava intercalations, breccia and scoria, we used the values of 5 GPa, 3 GPa, 1 GPa and 0.5 GPa, respectively. All the deposits were given a constant Poisson's ratio of 0.25 and density values of ρ_S=2600 kg/m^3 for the stiff lava deposits and ρ_C=2300 kg/m^3 for the compliant pyroclastic deposits (Babiker and Gudmundsson, 2004; Gudmundsson, 2012).

For our mechanical interpretations, we used the stiffness ratio contrast of the contacts for both the western (C_{w1} - C_{w6}, Fig. 4a) and eastern (C_{E1} - C_{E3}, Fig. 4b) sites and especially a dimensional ratio ($r=E_U/E_L$) which is the Young's modulus of the upper layer divided by the Young's modulus of the lower layer (Kavanagh et al., 2006; Drymoni et al., 2020). The dyke has been modeled at each contact as shown in Fig. 4a,b. For the western site (Fig. 4a), we tested six contacts from the bottom to the top, as follows:

$r(C_{W1})$=L/HR= 10/30=0.3

$r(C_{W2})$=B/L=1/10=0.1

$r(C_{W3})$=L/B= 10/1=10

$r(C_{W4})$=MB/L= 3/10=0.3

$r(C_{W5})$=ML/MB= 7/3=2.3

$r(C_{W6})$=L/ML= 10/7=1.42

Similarly, for the eastern site (Fig. 4b) we tested the following mechanical contacts from the bottom to the top as follows:

$r(C_{E1})$=L/HR= 10/30=0.3

$r(C_{E2})$=T/L= 5/10=0.5

$r(C_{E3})$=L/T= 10/5=2

It is worth mentioning here that the western site is an order of magnitude larger in layer thickness than the eastern site; so, although the layers have the same Young's modulus values, the ratios represent the mechanical contrast of the contacts at different scales.

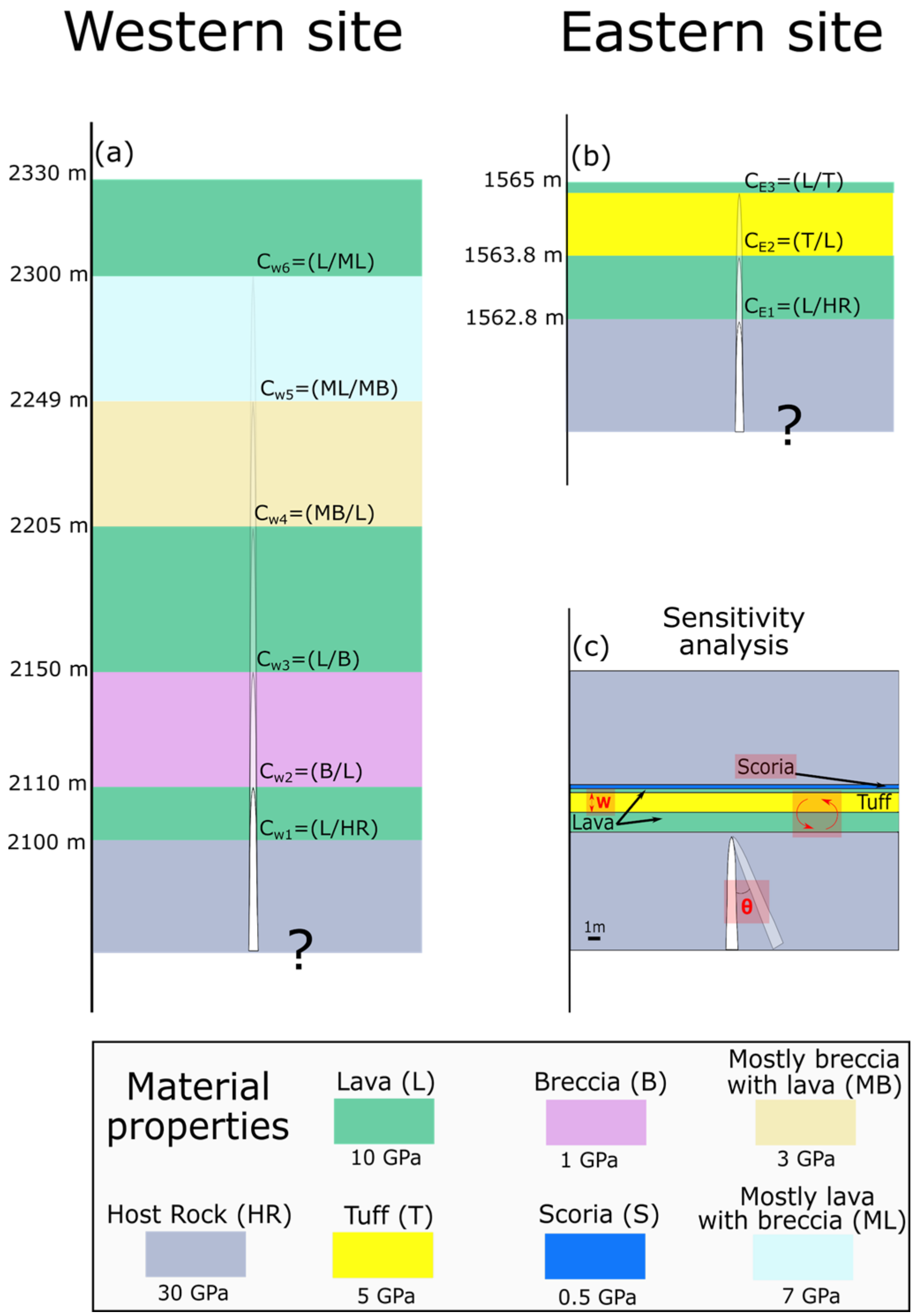

Figure 4. *Combined schematic stratigraphic logs showing the field-based stratigraphic sequence and thickness of the layers with the realistic material properties based on Gudmundsson (2011). The logs also visualise the numerical modelling concept followed here. While the dyke propagated in the crustal segments, snapshots were taken along its way on the mechanical dissimilar contacts (C_{W1} - C_{W6} for the western and C_{E1}*

- C_{E3} *for the eastern site, respectively). (a) The stratigraphic column of the western site is from Branca et al. (2011a), also shown in Fig. 2. (b) The stratigraphic column of the eastern site is from Tibaldi et al. (2022). (c) Schematic illustration of the eastern stratigraphic log showing the parameters studied in the sensitivity tests where W is the thickness of the layers and θ is the dip of the dyke. All of them are conceptualised in a direction orthogonal to the 1928 fracture system.*

3.2.2 Field-based model setups

In the present study, we designed numerical models through COMSOL Multiphysics (v5.6) (www.comsol.com). COMSOL is a Finite-Element-Method (FEM) software that investigates in 2D the distribution of dyke-induced local stresses and strains subject to user-defined dynamic boundary loads in a layered elastic medium. In our case study, we use the Structural Mechanics module to analyse the local stresses, such as the tensile (σ_3) and shear stress (τ), induced by a dyke in two mechanically heterogeneous crustal segments on Etna volcano. Through the software, we can discretise the area and divide the solutions into several elements that are then combined to give results that address the whole research question. The results approximate the differential equations posed initially (Deb, 2006; Masterlark and Tung, 2018). Here, we assess the concepts of Mode I, II fracturing and faulting (Broek, 1982; Gudmundsson, 2011) and the likelihood of the 1928 dyke propagation path.

We designed two heterogeneous computational domains, which were 2330 x 2330 m, 50 x 50 m and represented the western site and eastern and the sensitivity analyses' model setups, respectively (Fig. 5). This is because our layers on the western site are in the order of some meters (maximum 55 m), and the layers in the eastern site are in the order of some decimeters and meters (maximum 1 m). For the western part we used a size that refers to the absolute elevation of the stratigraphic sections, whereas the eastern size was selected arbitrarily after several tests so as to be most suitable for the models. The domains have been discretised by an extremely fine triangular meshing, with a minimum element size of 0.0466 m for the western site, and a minimum element size of 0.001 m for the eastern part and the sensitivity tests.

The dyke is modelled as an elliptical cavity with an internal overpressure (or driving pressure in excess of the normal stress σ_n on the rupture plane, for a dyke σ_3) range of P_o = 1-10 MPa. We use this range of overpressure values for four reasons. First, it is known from previous studies (Gudmundsson, 2012) that dykes in stratovolcanoes are injected from various depths and sometimes even from deep-seated reservoirs where the buoyancy term is positive because the density of the crust is higher than that of the basaltic magma. Therefore, to simulate those high overpressure conditions, we assigned a driving pressure of 10 MPa to the models. Also, based on analytical equations (Gudmundsson 2011), the dyke overpressure is proportional to the dyke thickness. Previous studies in dyke swarms emplaced at shallow depths at composite volcanoes have shown that the 90% of the overpressures typically range between 1-6 MPa (Drymoni et al., 2020). For this reason, we used the values of 1 MPa and 5 MPa for a constant shallow crust stiffness of the order of 5 GPa. Furthermore, the overpressure of a dyke is also related to the strike dimension (length) (Gudmundsson, 2011). Scudero et al. (2019) calculated the excess pressure of the magma chamber based on the lengths of the eruptive fissures and fractures and the thickness of the exposed dykes in the Valle del Bove. Their results proposed an averaged value of P_e=4 MPa, which is similar to the in-situ tensile strength (T_o) of the magma chamber roof at the time of the rupture (Barabási and Albert, 1999; Gudmundsson, 2020). Analytical studies (Gudmundsson, 2011) have shown that the overpressure is usually higher but close to the excess pressure values; hence an overpressure value of 5 MPa is realistic. Last but not least, some eruptive style changes (effusive to phreatomagmatic) are reported in other similar fissure events at Mt. Etna, close to our case study, such as the 1809 lateral feeder dyke (Geshi and Neri, 2014) and the Montagnola 1763, 1910 and 1983 eruptions (Kieffer, 1983; Tanguy, 1981). At very shallow levels, such eruptive interchanges can relate to gas exsolution mechanisms in basaltic magmas (Greenland et al., 1985) and can produce gas-rich flank eruptions. Thus, it can be attributed to rapid decompression in the conduit (Geshi and Neri, 2014), variable conduit geometry (diameter) or temporary conduit blocking (Murray and Pullen, 1984). For the fragmentation concept, we do not know if these dynamic changes could affect the overpressure of the dyke at that depth and scale. Still, we hypothesise that our studied range (P_o=1-10 MPa) can satisfy all four concepts mentioned above. At this point, we need to highlight that the results show similarities for the three different dyke overpressures in terms of the interpretation of the stress trajectories but, gradually, the magnitude and distribution of stresses are rising proportionally to the overpressure value for constant host rock mechanical properties and dyke length since the program uses equations of linear elastic materials. The same applies to the distribution of the stresses if we modify the size of the dyke; hence, we always keep a constant length value, which is up to half of the modelling domain, to eliminate this effect between the models.

Similarly, we chose a local extensional stress field range of F_{ext} = 0.5 - 2 MPa. This reflects the existence of active faults with strong deformation patterns in the close vicinity of the studied area. Specifically, the 11-km-long Pernicana Fault (Fig. 1b) is located at the NE tip of the rift and is very close to the studied eastern site (about 2 km). The fault has had very high slip rates, which reached 2.7 cm/yr during the Late Pleistocene-Holocene (Tibaldi and Groppelli, 2002). Similar values have been found at present by GPS measurements (Palano et al., 2009). For this reason, we applied a local 2 MPa horizontal extension to our models on the eastern site to replicate the effect of a strong local extensional stress field due to the fast eastward motions along the Pernicana Fault. However, since the western part of the 1928 fissure is further away from the fault and is practically only affected by the extension internal to the sliding block of the eastern volcano flank, we chose to use the value of 0.5 MPa. The selected values are based on empirical comparisons with other case studies (e.g., Feuillet 2013). This is consistent with the GPS vectors that report a decrease from NE to SW and indicate a decrement in the volcano flank slipping towards the same direction (Bonforte et al., 2007; Palano et al., 2009; Palano, 2016). Since the dyke intrusion propagated practically instantly in contrast to the annual deformation rate based on the active fault slip, in the sensitivity analysis, we used both values to simulate the different active stress fields at different timescales.

The dyke in our models is located in the central part of the domains (Fig. 5). This is because we intended to ensure an adequate distance from the model edges and exclude edge effects from our interpretations but also make sure that the stress field variations due to the dyke could be neglected. Although the dimensions of the domains were chosen to reproduce the realistic depths of the stratigraphic columns, we took one more precaution to ensure that the models are not affected by the boundary conditions of the models locked at the corners of the box. Specifically, we fastened only the models' bottom corners, leaving the top corners free to ensure that the upper part where the dyke is located can move freely and cannot be affected by the edge effects (Browning et al., 2021; Geyer and Gottsmann, 2010).

The layers within the rock domain have been modelled to behave elastically since experimental analyses have proven that solid rocks exposed on the crust at low strain conditions behave accordingly (Gudmundsson, 2011, 2020). In our models, we plotted the minimum principal compressive or maximum tensile stress (σ_3) as a colour scale and the absolute (von Mises) shear stress (maximum shear stress at the xy plane) as line contours to explore the distribution around the tip and the location of the highest concentrations, respectively. We also designed two arrow surfaces corresponding to the σ_1 and σ_3 principal compressive stress trajectories. To estimate the fracturing condition and the possibility of pre-existing fractures to slip we used fracture criteria based on Linear Elastic Fracture Mechanics (LEFM) (Broek, 1982). In particular, for Mode I and II fractures to be formed, the local stresses reach specific values. Tension fractures can be formed if the local absolute tensile stress (σ_3) gains a minimum of 2-5 MPa, which are the typical tensile strength (T_o) rock values (Amadei and Stephansson, 1997; Gudmundsson, 2011). Faults, however, can be formed when the shear strength is two times the tensile strength ($\tau > 2\sigma_3$), namely, 4-8 MPa (Kanamori and Anderson, 1975; Haimson and Rummel, 1982; Schultz, 1995).

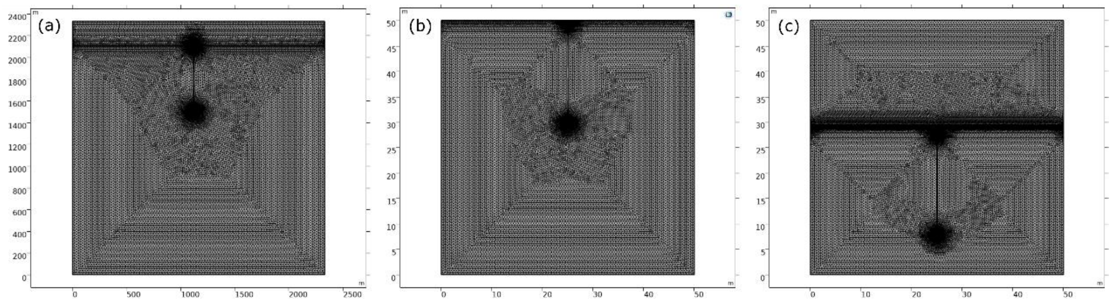

Figure 5. *COMSOL model setups. (a) The domain of the western site has dimensions of 2330 x 2330 m and the vertical dyke (black line) is 800 m; (b) the domain of the eastern site has dimensions of 50 x 50 m and the vertical dyke is 20 m; (c) The domain of the sensitivity tests has dimensions of 50 x 50 m and the vertical dyke is 20 m..*

3.2.3 Sensitivity tests

We performed several sensitivity tests by varying the layer thickness (W), the layer sequence, and the dyke dip to investigate how the influence of these parameters or their combinations might affect graben formation (Fig. 4c). In detail, the latter gave us insights into how the layers' stratigraphy, the dyke, and layers' geometrical parameters can affect the dyke-induced graben formation. We made the following tests for the same two overpressure concepts, namely 1 MPa and 5 MPa, to explore the effect of specific parameters based on field observations (Tibaldi et al., 2022) and previous studies (Tibaldi and Groppelli, 2002). For the parametrisation, we reduced the thickness of the upper lava from 0.2 m to 0.1 m to allow our modelling method to explore the parameters at different orders of magnitude (0.1 m and 1m). Evidence of scoria deposits has been proposed near the eastern site; thus, our sensitivity analysis explored the effect of very soft pyroclastics on the stratigraphy. Finally, we tested the effect of an inclined sheet by dipping the vertical dyke and changing the stratigraphic sequence simultaneously. The final studied concepts are shown below:

1. Increasing the thickness of the top lava layer by one order of magnitude (from 0.1 to 1 m).
2. Changing the stratigraphic sequence by moving the tuff deposit at the bottom of the succession.
3. Adding a 1 m scoria layer atop the original stratigraphic sequence.
4. Adding a 0.1 m scoria layer atop the original stratigraphic sequence.
5. Adding a 1 m scoria layer at the bottom of the original stratigraphic sequence.
6. Adding a 0.1 m scoria layer at the bottom of the original stratigraphic sequence.
7. Adding a 1 m scoria layer atop the original stratigraphic sequence and changing the dip of the dyke from 45° to 90°.
8. Adding a 0.1 m scoria layer atop the original stratigraphic sequence and changing the dip of the dyke from 45° to 90°.

Finally, we arbitrarily assessed the accumulation and distribution of stresses around the dyke tip and the layers according to the following criteria. For the minimum principal compressive or maximum tensile stress (σ_3) values:

- Low concentration:1-2 MPa;
- Moderate concentration: 3-7 MPa;
- High concentration: 8-10 MPa.

For the von Mises shear stress (τ) values:

- Low concentration: 1-3 MPa;
- Moderate concentration: 4-8 MPa;
- High concentration: 9-12 MPa.

For the absolute shear stress (τ) distribution:

- Low: the contours are generally concentrating below the tip and at the studied contact;

- Moderate: the contours are generally concentrating symmetrically around the tip and at the studied contact;
- High: the contours are generally concentrating symmetrically around the tip and above the studied contact.

4. Numerical modelling results

We designed models in heterogeneous shallow crustal segments, namely the western and eastern sites, to explore the mechanical conditions needed for the dyke to form tension fractures and/or faults at the surface. Specifically, we modelled how the dyke propagated to the surface by studying the sequence of the realistic mechanically contrasting contacts from depth to the surface. We aimed to explore: 1) the concentration of tensile stress at the propagating dyke tip, its distribution and range; 2) the spatial distribution of the shear stress around the propagating dyke tip, as well as its quantitative build-up towards the surface; 3) the possible propagation path of the dyke, as shown by σ_1 and σ_3 trajectories ahead of the ascending tip, based on the studied boundary conditions.

As a first step, we qualitatively compared the models in terms of tensile stress concentration ahead of the tip and inside the dissimilar layers. Secondly, we compared the models' shear stress spatial distribution contours near the tip and traced the probable location of fault slip ahead of the dyke tip and closer to the upper part of the domain. This condition assumes that in our models, dyke-induce faulting nucleates at the surface (Al Shehri and Gudmundsson, 2018; Bazargan and Gudmundsson, 2019; von Hagke et al., 2019). Also, we compared the rising values of shear stress towards the surface and denoted the parameters that increase them in our models. Finally, we investigated the mechanical conditions (and contacts) that could have encouraged stress barriers in the layered domains.

4.1 Western site with P_o=1-10 MPa and F_{ext}= 0.5 MPa

In the first three models (A-C) (Fig. 6), the dyke was at the lowest contact of the stratigraphic sequence (C_{W1}). We gradually increased the overpressure of the dyke from 1 MPa, then to 5 MPa and finally to 10 MPa while we kept constant the horizontal extension (F_{ext}= 0.5 MPa). In model A, the tensile stress accumulated mainly at the tip of the dyke and the thin lava layer above it. Low tensile stress concentration was observed in the upper lava layer but not in the soft pyroclastic layers. This is a common outcome in layered sequences because stiff layers in nature tend to concentrate stresses more than compliant ones, which instead they tend to suppress them (Gudmundsson, 2011). The shear stress was low since the contours were concentrated at the studied contact and below it. Stress rotations occurred in the soft breccia layer, which could implement dyke-arrest. In model B, the tensile and shear stress increased proportionally to the overpressure compared to model A. However, neither the tensile stress nor the shear stress concentrated at the top of the succession; instead, the shear stress contours became wider. We still observed stress rotations in the breccia layer. Finally, model C showed high tensile and shear stress concentrations close to the tip, and the breccia layer kept acting as a temporary stress barrier in the stratigraphy. The shear stress contours in this scenario did not approach the top layers keeping a similar but wider distribution.

The dyke was now moved to the next contact between the breccia and the lava layers (C_{W2}). Similarly, to model A, the breccia layer in model D suppressed the tensile and shear stresses at the tip. Stress rotations were observed only at the stiff/soft (lava/breccia) contact above but not inside the breccia layer. Hence, an arresting concept at the contact was still possible. The tensile and shear stress concentration increased when we raised the overpressure (model E) while the stress rotations at the contact above remained the same. Finally, in model F we observed similar results with the previous models (D and E). The shear stress contours, however, intersected the breccia and lava layers but could not move upper in the succession.

As a next step, we moved the dyke to the third contact (C_{W3}), which practically represented the highest mechanical contrast of the succession. In model G, both the tensile stress is concentrated mainly at the lava layer above the tip, but also the shear stress was greatly suppressed. In this case, no stress rotations were observed at the soft layers. In models H and I, we observed an accumulation of high tensile stress in the lava layer. When we increased the overpressure, the shear stress contours were distributed higher and wider inside the lava layer, similar to model F.

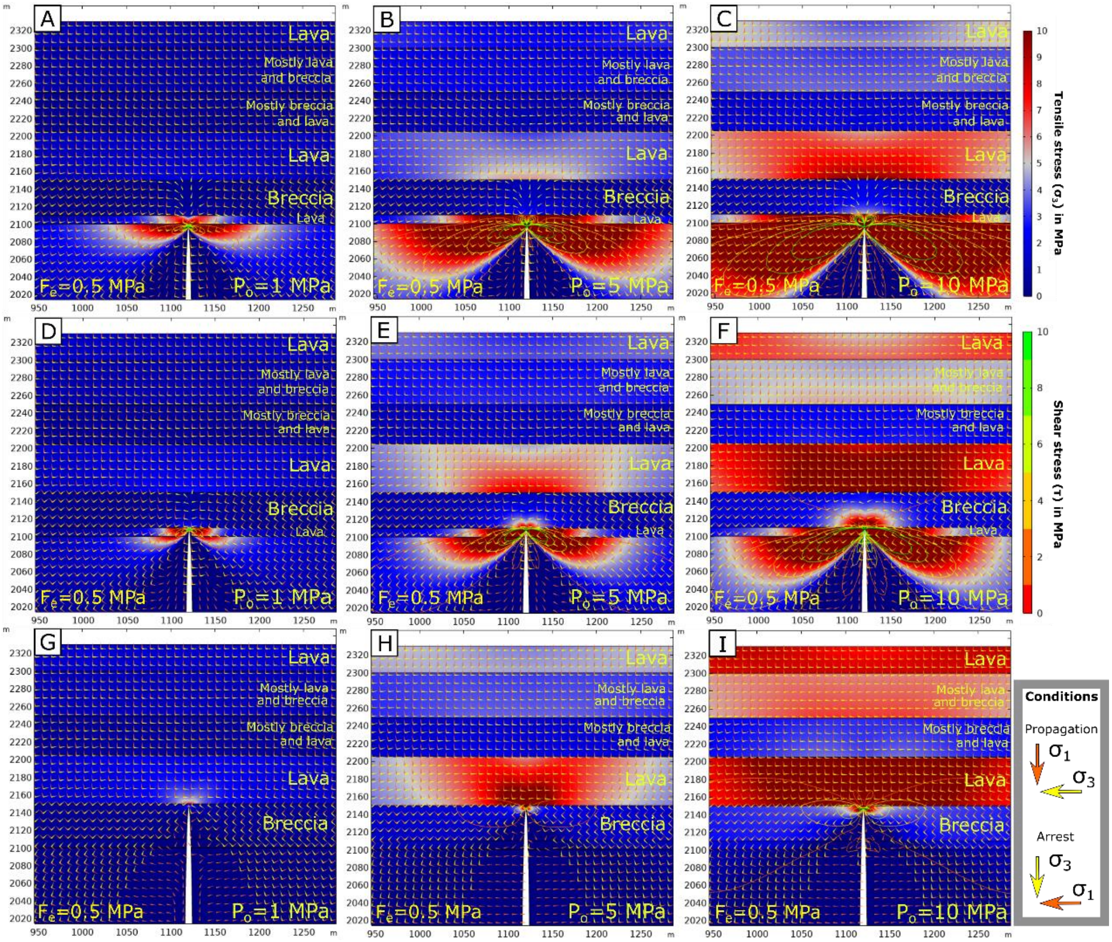

Figure 6. *COMSOL models based on the stratigraphy of the western site. In all models, we applied the same boundary conditions, which are three overpressure values, namely 1 MPa (A,D,G), 5 MPa (B,E,H) and 10 MPa (C,F,I) and a local extensional stress field of 0.5 MPa. The graphical conditions for arrest/propagation are shown in the key inset. A-C are Models of the Cw$_1$ contact, D-F are Models of the Cw$_2$ contact, G-I are Models of the Cw$_3$ contact. The distribution of the minimum principal compressive or maximum tensile stress (σ_3) is shown with the colour scale bar, while the spatial and quantitative distribution of absolute shear stress (τ) (von Mises in xy plane) is shown with the contour lines. σ_1 trajectories are shown with orange arrows and σ_3 trajectories are shown with yellow arrows.*

Moving to the next contact (C$_{W4}$) (Fig. 7) in model A, where the overpressure is 1 MPa, the tensile and shear stress concentration was low. The shear stress contours were distributed below the studied contact. In this model, stress rotations also formed in the layer atop, but they were insufficient (≤90°) to satisfy an arrest condition. Models B and C showed higher shear and tensile stress accumulation. Especially in C, the shear stress distribution is wider. We consider that rocks usually break between 0.5 and 9 MPa (Amadei and Stephansson, 1997), which are the tensile strength values in the crust. In that case, this condition could imply that tension fractures were likely to form at the surface. Still, no 90° stress rotations occured in the soft layers ahead so the dyke was likely to propagate to the surface. In the next contact (C_{W5}), when the overpressure was low (model D) and the mechanical contrast was high (stiff/soft), the shear and tensile stresses were significantly suppressed and low, respectively. Once the overpressure (models E and F) increased, the tensile stress was concentrated on the stiff lavas atop the dyke tip. No stress rotations occurred at the contacts or layers. The shear stress distribution in model E was similar to model B. In models C, E, F, and H the shear stress distribution reached the top of the succession, so tension fracture conditions were met. Finally, at the top contact (C_{W6}), all models (G-I) showed significant similarities with the models D-F. Still, when the overpressure was 10 MPa (model I), the shear stress contours had a wider distribution towards the surface and a graben could be formed.

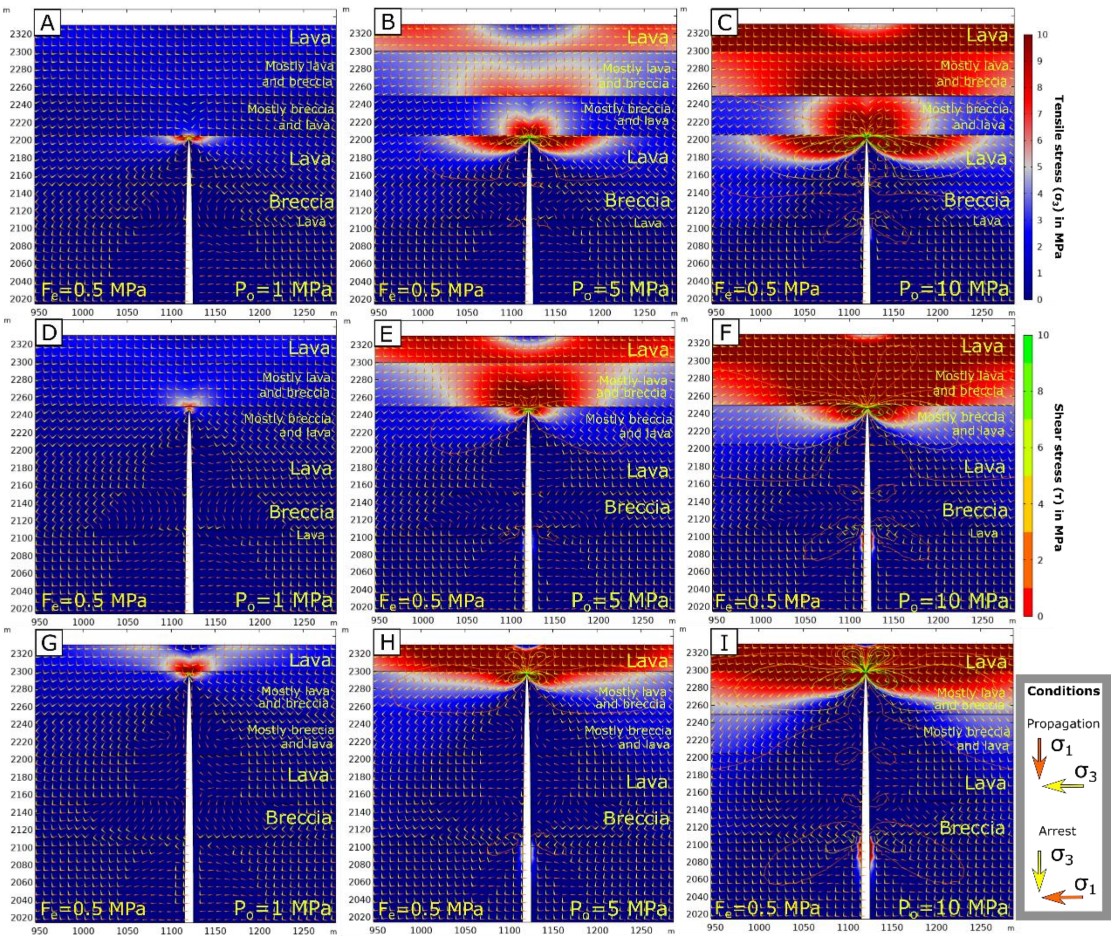

Figure 7. *COMSOL models based on the stratigraphy of the western site. In all models, we applied the same boundary conditions, which are three overpressure values, namely 1 MPa (A,D,G), 5 MPa (B,E,H) and 10 MPa (C,F,I) and a local extensional stress field of 0.5 MPa. The graphical conditions for arrest/propagation are shown in the key inset. A-C Models of the* Cw_4 *contact, D-F Models of the* Cw_5 *contact, G-I Models of the* Cw_6 *contact. The distribution of the minimum principal compressive or maximum tensile stress (*σ_3*) is shown with the colour scale bar, while the spatial and quantitative distribution of absolute shear stress (*τ*) (von Mises in xy plane) is shown with the contour lines.* Σ_1 *trajectories are shown with orange arrows and* σ_3 *trajectories are shown with yellow arrows.*

We have calculated, separately, the von Mises shear stress (τ) (Fig. 8) and the tensile stress (σ_3) concentration (Supplementary 1) at the different contacts as the dyke propagates towards the surface. In Figure 8 we present the results for 5 MPa overpressure (models a-f) and an extra 0.5 MPa extension (models d-f). The models show a gradual shear stress increase towards the surface which satisfy the condition for graben formation ($\tau>2\sigma_3$). The stress curves show two shear stress maximums around the dyke tip which gradually get higher and their stress peaks narrower as the dyke propagates towards the surface. This is associated with the proximity to the surface and the dissimilar mechanical properties of the layers (Bazargan and Gudmundsson, 2019).

Here, we have also examined how layers with variable thickness values and the local extension affect the tensile and shear stress distribution of a propagating dyke. The stress curves show that the surface stresses increase as the dyke gets shallower and their peaks are related to the depth of the dyke as previous studies have shown (Al Shehri and Gudmundsson, 2018). Finally, the extensional stress field increases the tensile and shear stress accumulation at the tip and at the surface, respectively (models 9c and 9f). Similar results we observe for the tensile stress distribution as well (Supplementary 1).

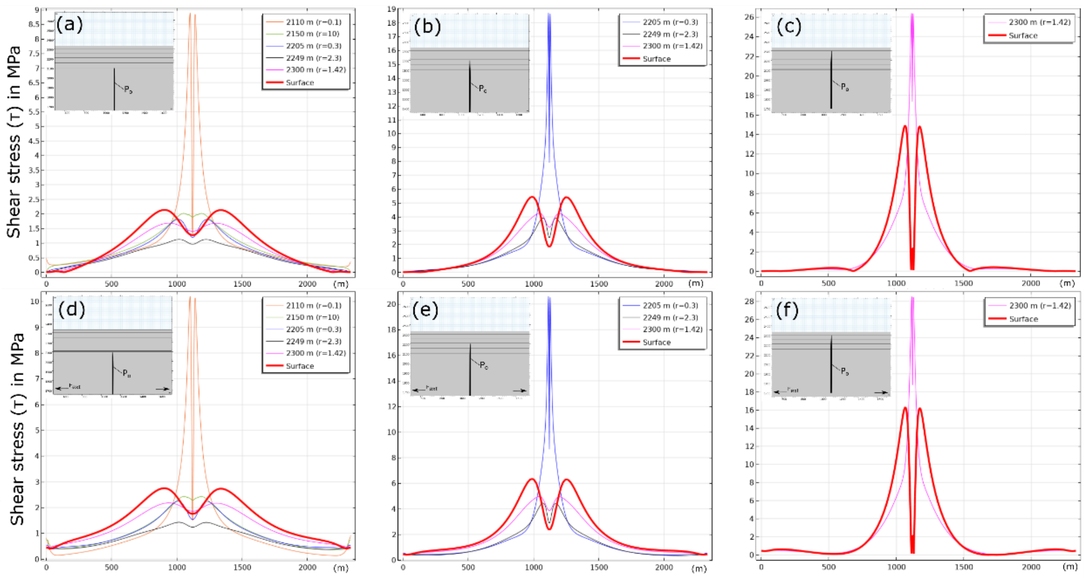

Figure 8: COMSOL 1D line plots showing the von Mises shear stress (τ) concentration at the different contacts while the dyke propagates towards the surface (western graben). All the models (a-f) have 5 MPa overpressure (P_o). In models d-f an extra extensional boundary load (F_{ext}=0.5 MPa) is applied. Surface denotes the contact between the top layer and the atmosphere.

4.2 Eastern site with P_o=1-10 MPa and F_{ext}= 2 MPa

We modelled the first contact C_{E1} in the first model runs, with rising overpressure values and constant local horizontal extension (F_{ext}=2 MPa). All models' results are shown in Figure 9. In Model A, we observed a high tensile stress concentration ahead of the tip and in the stiff lava contacts. We gradually increased the overpressure from 1 MPa to 5 MPa and finally (one order of magnitude) to 10 MPa. In that case, the tensile stress was proportionally increased around the tip and towards the top of the succession. The σ_1 and σ_3 trajectories showed no stress rotations in the soft layer. The shear stress built up spatially and quantitatively, proposing tension fractures at the surface in models B and C.

We moved to the following contact (models D-F) between the tuff and the lava (C_{E2}). Here we observed similar results as in the bottom (C_{E1}) contact. The only difference was that higher tensile stress accumulation inside the tuff layer. The shear stress contours had a similar distribution but were higher in the succession. No stress rotations occurred in any of the models.

Finally, we tested the dyke at the top contact C_{E3} (models G-I), which corresponded to the top contact between the lava and the tuff. The models showed similarities with the previous models (A-C and D-F) regarding the accumulation and distribution of the tensile and shear stresses, respectively. Here, in the first model triplet, we assigned to the host rock the same value used in all models ($E_{host\ rock}$=30 GPa). However, in these model runs, no stress rotations were formed. In the last triplet, we assigned to the host rock a low Young's modulus value (Ehost rock=1 GPa) to simulate a very soft host rock segment. The models showed that when the overpressure was low (Po= 1 MPa), the tensile stress concentration was lower, and the shear stress distribution reached the surface. The results in models K and L were similar to models H and I. No stress rotations occured in any of the models (J-L).

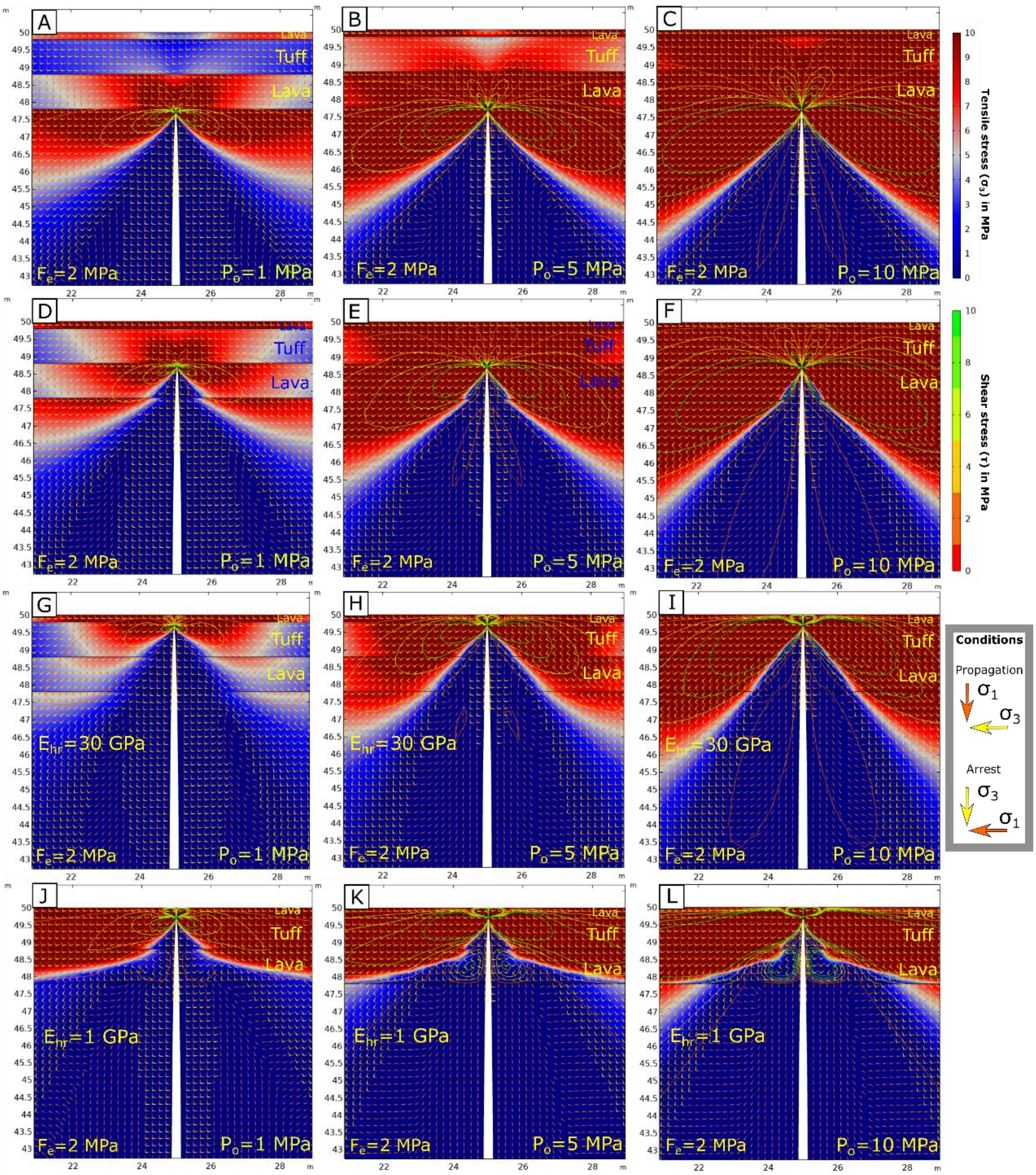

Figure 9. *COMSOL models based on the stratigraphy of the eastern site. In all models we applied the same boundary conditions which are three overpressure values, namely 1 MPa (A,D,G,J), 5 MPa (B,E,H,K) and 10 MPa (C,F,I,L) and a local extensional stress field of 2 MPa. The graphical conditions for arrest/propagation are shown in the key inset. A-C Models of the* C_{E1} *contact, D-F Models of the* C_{E2} *contact, G-I Models of the* C_{E3} *contact J-L Models of the* C_{E3} *contact with host rock stiffness of 1 GPa. The distribution of the minimum principal compressive or maximum tensile stress (*σ_3*) is shown with the colour scale bar, while the spatial and quantitative distribution of absolute shear stress (*τ*) (von Mises in xy plane) is shown with the contour lines.* Σ_1 *trajectories are shown with white arrows while* σ_3 *trajectories are shown with black arrows.*

We have similarly plotted the shear stress (Fig. 10) and tensile stress (Supplementary 2) curves at the different contacts as the dyke propagates towards the surface. Here, since the dyke is almost reaching the surface, the tensile and shear stress values of our models are very high. Such values are not realistic since rocks can break as soon as they reach the in-situ tensile strength (T_o) threshold (Gudmundsson, 2011). The graphs serve mostly as a theoretical investigation. We observe again the two maximum peaks that surround the tip to get narrower. Also, contacts with higher stiffness ratios concentrate higher stresses while the dyke approaches them.

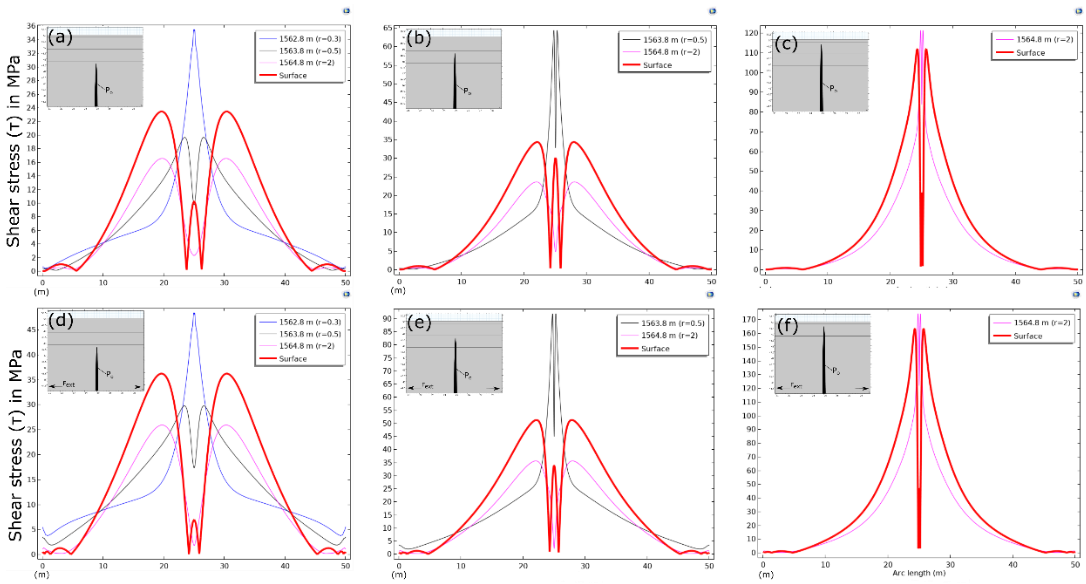

Figure 10: COMSOL 1D line plots showing the von Mises shear stress (τ*) concentration at the different contacts while the dyke propagates towards the surface (eastern graben). All the models (a-f) have 5 MPa overpressure (Po). In models d-f an extra*

extensional boundary load (Fext=0.5 MPa) is applied. Surface denotes the contact between the top layer and the atmosphere.

4.3 Sensitivity tests with P_o=1 MPa and F_{ext}= 2 MPa

For the sensitivity analyses, we modelled a vertical dyke with an assigned overpressure of 1 MPa in a heterogeneous crustal segment and a stiffness range of 0.5-30 GPa. The model outcomes are seen in Figures 11 and 12, and their interpretation is as follows.

The first model runs showed the studied concepts reported in 3.2.3 with constant boundary conditions, namely P_o=1 MPa and F_{ext}= 2 MPa. In model A, we kept the same stratigraphic sequence but, instead, we increased the thickness of the top lava layer by one order of magnitude (from 0.1 to 1 m). In the model, we observed 90° stress rotations at the tuff layer and almost up to 45° at the lava layer. The accumulation of tensile stress was high at the dyke tip and the stiff lava layers and moderate at the tuff. The shear stress distribution was low to moderate ahead of the tip. In model B, we moved the tuff layer at the bottom of the stratigraphy. Both the tuff and the top lava layer had around 45° stress rotations, the tensile stress increased in all the layers, and the shear stress distribution remained low to moderate. In models C and D, we explored the effect of a very soft pyroclastic layer at the top of the succession, such as scoria. In the first case, the thickness of the scoria was 1 m, while in the second case it was thinner by one order of magnitude (0.1 m). The models showed that the tensile concentration is high around the tips in both cases. However, we observed 90° stress rotations in the thick scoria layer in model C. The thin scoria and lava layers and the lava/tuff contact had similar stress rotations in model D. The thick scoria layer suppressed the tensile and shear stress from lower to moderate values without being distributed higher. Instead, the thin scoria layer could not suppress the tensile stress similarly.

We tested the existence of a thick and thin scoria layer at the bottom of the column. The thick scoria layer (model E) could promote stress rotations at the tuff/scoria contact, whereas no stress rotations occurred in the second case (model F). We finally observed low tensile stress concentration at the scoria layers. The shear stress was moderate to high in both models. We changed the dip of the dyke for the last sensitivity concept while keeping a thick (model G) and a thin (H) scoria layer at the top of the stratigraphy. Our models have shown that the shear stress is low when the scoria is thick, instead, in thin scoria model runs, the shear stress values around the tip are higher and asymmetrically in both cases. That could imply the formation of semigraben at the surface. In both models (G and H), we observed no 90° stress rotations at the scoria layers so the dyke could not arrest on its way.

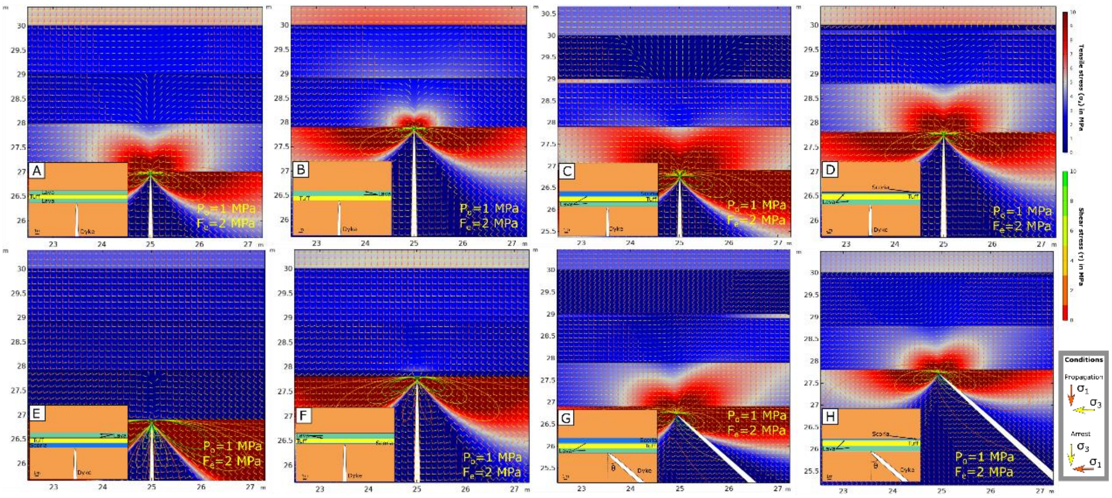

Figure 11. *Sensitivity tests based on the stratigraphy of the eastern site. In all models, we applied the same boundary conditions, which is an overpressure value of 1 MPa and a local extensional stress field of 2 MPa. The distribution of the minimum principal compressive or maximum tensile stress (σ_3) is shown with the colour scale bar, while the spatial and quantitative distribution of the absolute shear stress (τ) (von Mises in xy plane) is shown with the contour lines. Σ_1 trajectories are shown with orange arrows while σ_3 trajectories are shown with yellow arrows. The graphical conditions for arrest/propagation are shown in the key inset. A – H are the concepts as illustrated in the index box.*

4.4 Sensitivity tests with P_o=5 MPa and F_{ext}= 0.5 MPa

We reran the suites of the sensitivity concepts by changing the boundary conditions to P_o=5 MPa and F_{ext}= 0.5 MPa to simulate a dyke with higher overpressure but during a period where the local extensional stress field is lower (Fig. 12).

In model A, both tensile and shear stress were high in the vicinity of the dyke tip. We also observed 90° stress rotations at the tuff, hence suggesting the scenario of a dyke that gets arrested in-depth but still could satisfy the fracturing (and possibly faulting) concepts at the surface, in a similar way to dyke-induced graben formation. In model B, the stress rotations were also 90°, and the tensile and shear stresses were high. Moving to model C, the thick scoria layer had 90° stress rotations. Similarly, when the scoria layer was thin, there was a higher accumulation of shear and tensile stress at the top of the succession. Finally, stress rotations occurred at the tuff and scoria layers (model D). In models, E and F, where the thick and thin scoria layers were at the bottom of the stratigraphic sequence, tensile and shear stresses were high. The dyke is likely to be arrested in model E while it dissects the contact in model F. In the final models, we explored how inclined sheets would propagate in similar scenarios with higher overpressures than before (Fig. 12g, h). In model G, tensile and shear stress were asymmetrically high, and stress rotations occurred. Finally, in model H we observed again stress rotations in the tuff layer while the tensile and shear stresses were high and asymmetrical.

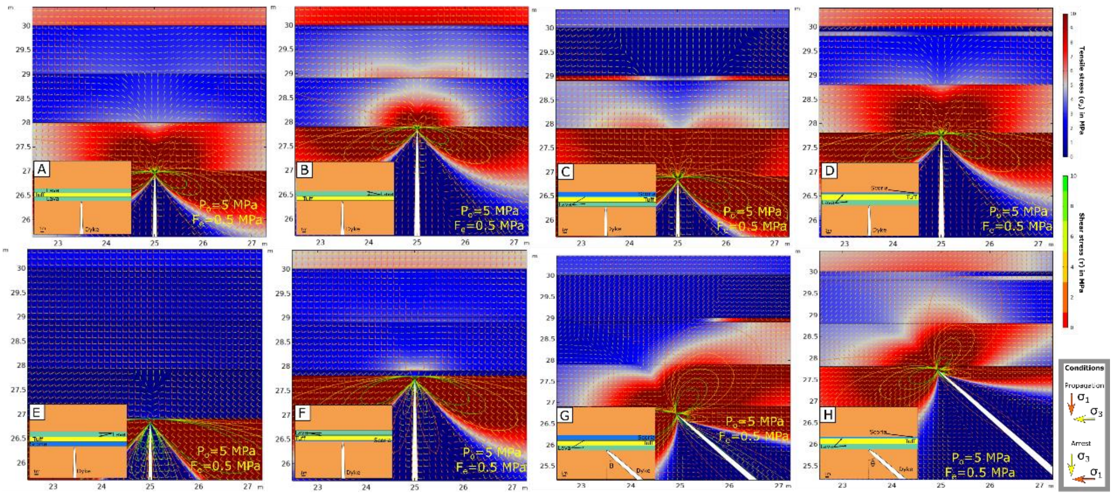

Figure 12. *Sensitivity tests based on the stratigraphy of the eastern site. In all models, we applied the same boundary conditions, which is an overpressure value of 5 MPa and a local extensional stress field of 0.5 MPa. The distribution of the minimum principal compressive or maximum tensile stress (σ_3) is shown with the colour scale bar, while the spatial and quantitative distribution of the absolute shear stress (τ) (von Mises in xy plane) is shown with the contour lines. Σ_1 trajectories are shown with orange arrows while σ_3 trajectories are shown with yellow arrows. The graphical conditions for arrest/propagation are shown in the key inset. A – H are the concepts as explained in the index box.*

4.5 Synthesis on dyke arrest / propagation and dyke-induced graben formation

In this section, we summarise the dyke propagation paths resulting from modelling the western and eastern sites. We present two graphic illustrations (Fig. 13) representing the probability of arrest/propagation and dyke-induced graben formation in the two heterogeneous successions.

Specifically, in Figure 13a, we assess the likelihood of propagation or arrest at the western site. On the X-axis, we present the ratio (lowest to highest) of the mechanical contrast of the layers subject to rising overpressure values (Y-axis) based on Figures 6 and 7. We observe that the contacts with low mechanical contrast (r = 0.1 - 0.3) are more likely to promote dyke arrest scenarios than those with higher mechanical contrast (r = 1.42 - 10). We report that the contact C_{W1} (lava/host rock) and the contact C_{W4} (breccia/lava) have similar mechanical ratios but different dyke paths. Similarly, in Figure 13b, we highlight the modelling results of the eastern site. The latter shows that all contacts promote dyke propagation, mainly because the stratigraphy is very shallow. We rerun the same models with the stratigraphy in the middle of the domain and the tuff layer had stress rotations. Similarly, the contacts with low mechanical contrasts (r = 0.3 - 0.5) promote mostly arrest.

We also assessed the probability of graben formation ahead of the dyke tip based on the qualitative modelling results of the shear stress (τ) distribution. In the western site, we observe that if dyke-induced graben formation occurs when the shear stress concentration is high ahead of the tip (Tibaldi et al., 2022), then this concept is satisfied when the mechanical contrast of contact is over r = 0.3 and the dyke overpressure is high (P_o = 5-10 MPa). We point out that, although the contacts $C_{W4\text{-}6}$ are the ones found higher in succession, they are not close to the side edges, so the models are not affected by edge effects, however, they are close to the upper host rock domain.

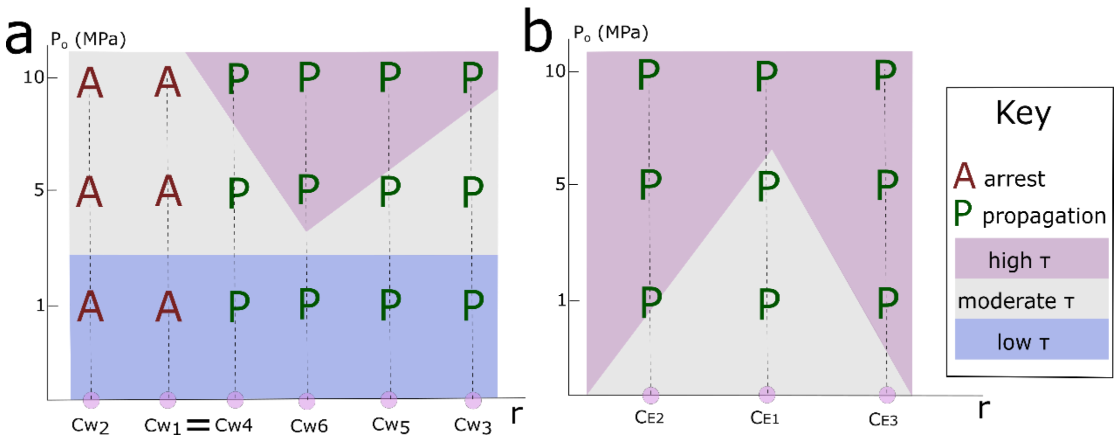

Figure 13. *(a) Schematic illustration of the dyke propagation paths and the concentration of shear stress around the tip on the western site based on the models of Figures 6 and 7. X-axis the contact in increasing mechanical contrast, Y-axis the overpressure value. (b) The same results from the eastern site based on the models of Figure 9.*

5. Discussion

Our models attempt to gain insights into the processes that controlled the surface deformation during the 1928 fissure eruption. In particular, we aim to understand the parameters that could have promoted the dyke-induced graben and fissure eruption in the western site and the semigraben and graben in the eastern one. To achieve this goal, we designed suites of sensitivity tests to explore key geometrical parameters.

In detail, we modelled the effect of layer thickness, the presence of soft layers in the stratigraphy at the top and bottom of the column (varied sequence), the dyke tip, and their combination. Below are the results for each suite.

Stratigraphic sequence

The sensitivity suites show how efficiently the Young's modulus of the dissimilar layers and the stratigraphy can control the propagation path of a dyke. Our models have enabled to observe stress rotations in contacts with low stiffness contrast, particularly in the soft layers (breccia, scoria).

Layer thickness

The models suggest that changes of an order of magnitude (from 0.1 m to 1 m) in layer thickness could promote stress rotations. However, in the models the most crucial parameter remains the stiffness of the layers.

Dyke dip

Our results have shown that temporary stress barriers can be formed in soft layers (e.g., scoria, breccia) if inclined sheets (≤ 75° dip) are increasing their dip.

5.1 Surficial deformation concepts

We performed a final synthesis of the sensitivity models shown in Figures 11 and 12, and we reported the likelihood of each studied concept. Specifically, we interpret the possible surficial deformation structures based on the physics-based in-depth models. Those are developed according to three studied indications: i) the concentration of tensile stress that has to be at least equal to the tensile strength of the crustal rocks (1-9 MPa) for fracturing (Amadei and Stephansson, 1997; Gudmundsson, 2011), ii) the concentration of shear stress that has to be usually two times the tensile strength of the rocks (normally 4-8 MPa) for fault slip (Kanamori and Anderson, 1975; Haimson and Rummel, 1982; Schultz, 1995), and iii) the formation of stress barriers for dyke arrest or for hampered dyke propagation. All of them are assessed at the top contact.

The analyses have shown that dyke-induced graben formation is associated with high tensile and shear stress concentration (> 4 MPa) (need not coincide e.g., Bazargan and Gudmundsson, 2019) at the surface and in the vicinity of the tip. The dyke in this concept should arrest (stress barriers) during ascent. A dyke-induced graben can be accompanied by a fissure eruption if, in the last case scenario, the dyke overcomes the temporary stress barriers or finds none of those on its way to the surface. Thus, the dyke can also feed an eruption. Similarly, a semigraben can be formed when an inclined sheet propagates towards the surface following the above stress concepts. Finally, according to our FEM model interpretations, narrow grabens can be encouraged if the stratigraphy includes soft layers such as scoria, breccia, or tuffs and the dyke overpressure is high (P_o = 10 MPa). Wider grabens are formed when the stratigraphy is composed mainly by stiffer materials such as lavas and the dyke overpressure is moderate (P_o = 5 MPa).

Tension fractures can possibly form at the surface when only the fracturing (tensile stress) concept is satisfied, and the tensile stress distribution is reaching the surface. Fault slip (here, we only hypothesise that it relates to pre-existing fractures, not the generation of new ones since their location and energy conditions are still challenging to be forecast, Backers and Stephansson, 2012) could occur if only the shear stress concept is satisfied. Again, the stress distribution has to reach the surface (but for our physics-based models the top contact in particular). Based on the above concepts, we hereunder provide qualitative interpretations of the sensitivity models, which are shown in the following table.

Table 1. *Qualitative analysis of the sensitivity models from Figures 11 and 12 showing the possible projected outcomes if the tensile and shear stress concentration can reach the surface (here the topmost contact). The tensile and shear stress curves are found in Supplementary material 3 and 4.*

	P_o = 1 MPa and F_{ext} = 2 MPa	P_o = 5 MPa and F_{ext} = 0.5 MPa

Concept A	Dyke arrest/ tension fractures	Dyke arrest / dyke-induced graben
Concept B	Dyke arrest/ tension fractures	Dyke arrest / dyke-induced graben
Concept C	Dyke arrest/ tension fractures	Dyke arrest/ tension fractures
Concept D	Dyke arrest/ tension fractures	Dyke arrest/ tension fractures
Concept E	Dyke arrest/ tension fractures	Dyke arrest/ tension fractures
Concept F	Dyke arrest/ tension fractures	Dyke arrest / dyke-induced graben
Concept G	Fissure eruption/ tension fractures	Dyke arrest/ tension fractures
Concept H	Fissure eruption/ tension fractures	Dyke arrest / dyke-induced semigraben

The statistical analysis of the above numerical concepts suggests that dyke arrest in the eastern site is the most likely concept (14/16= 87.5%), followed by dyke arrest accompanied by tension fractures (10/16=62.5%), dyke arrest and dyke-induced graben formation (3/16=18.8%). The least possible concepts are represented by fissure eruption and tension fractures (2/16=12.5%), and dyke arrest and semigraben formation (1/16=6.25%)

In the field, we observed two deformation settings related to dyke arrest and dyke-induced graben /semigraben. Statistically, these two concepts individually are highly probable according to our FEM models. However, their combination is less likely. Dyke arrest and semigraben formation could be satisfied in a scenario similar to concept H. Finally, dyke arrest and dyke-induced graben formation could be satisfied by concepts A, B, F.

5.2 Dyke-induced graben conditions in heterogeneous volcanic successions

In nature, most dykes that successfully propagate to the surface commonly form tension fractures but not grabens (Al Shehri and Gudmundsson, 2018; Bazargan and Gudmundsson, 2019). This is because studies of arrested dykes in composite volcanoes have shown that the dykes that stall tend to thin out without generating tension cracks, faults or surface fractures around their tips (Gudmundsson, 2012; Geshi and Neri, 2014; Drymoni et al., 2020). Instead, feeder dykes can make it to the surface and form tension fractures if they meet stiff layers very close to the surface (Al Shehri and Gudmundsson, 2018).

Although both dykes and grabens are associated with extensional stress regimes, interdisciplinary studies have shown that dykes can either induce graben formation in the same volcanotectonic event or not (Opheim and Gudmundsson, 1989; Koehn et al., 2019). However, in the case of a synchronous propagation of a dyke and the generation of a graben, their co-existence does not necessarily mean that the graben was formed due to the interaction with the dyke because the graben may be entirely due to purely tectonic forces as occurred at Santorini volcano (Drymoni et al., 2022). This is because still, the conditions that encourage dyke-induced grabens are not yet fully understood and are occurring basically in very short (geologically instant) timescales compared to active tectonics (e.g., faults, sliding flanks, other dyke intrusions, plate movements) (Kolzenburg et al., 2022). Therefore, although dyke and graben formation overlap in timescales, their co-genetic interactions or interconnections cannot be traced when the dyke is still on the way to the surface.

On the other hand, structural geology and geophysics can only efficiently study part of the process. During unrest, geophysics can partly determine from seismic data and partly from geodetic surface data, in particular, InSAR and GPS data (Biggs et al., 2009; Ebinger et al., 2010; Ágústsdóttir et al., 2016) the location and velocity of the propagating dyke and forecast its outcome only when the latter is very close to the surface and, most of the times, it leads to an eruption (Biggs et al., 2013; Giampiccolo et al., 2020). Similarly, structural geologists can study the surface deformation during a dyke-induced graben event but only retrospectively after it has already occurred (Sigurdsson, 1980; Gudmundsson, 1987; Pallister et al., 2010; Neri et al., 2011; Tibaldi et al., 2020, 2022). Still, although they can document realistic post-process observations, the data cannot shed light on the mechanisms in depth, because the actual conditions are always unknown.

A great number of theoretical, analytical and modelling studies have been focused on exploring those enigmatic conditions of dyke-induced graben formation in homogeneous domains through 'crack opening concepts' (Dieterich and Decker, 1975; Pollard and Holzhauser, 1979; Pollard et al., 1983; Rubin and Pollard, 1988; Mastin and Pollard, 1988; Chadwick and Embley, 1998). Here, dyke propagation triggers cracks that coalesce to fractures in layered domains and subsequently induces surficial deformation related to pressure changes towards the surface (overpressure). Surface deformation produced by faults has been extensively studied through dislocation modelling in isotropic homogeneous half-space domains (Okada, 1985; Dahm, 1996; Bonafede and Danesi, 1997; Bonafede and Rivalta, 1999; Rivalta et al., 2019). Dislocation modelling explores the displacement related to dyking by extracting information regarding the position, depth and dyke geometry (Bonafede and Rivalta, 1999). Dyke-induced deformation, here, occurs due to constant opening. From a mechanical perspective, grabens are formed at the shear/tensile stress peaks and not at the localities where the surface deformation peaks. Surficial deformation can begin appearing at the surface if the dyke is less than one km in depth. For that reason, tension fractures form at the maximum tensile/shear stress overlapped locations at the surface; thus, the co-existence of tension and shear fractures are not often found above the dyke tip at the surface. A concept which is encouraged when the top layers are stiff (e.g. lavas) (Bazargan and Gudmundsson, 2019).

The graben faults in nature usually dip 60-80° or are almost vertical, whereas in numerical applications are found to dip around 40-60° (Gudmundsson, 2017). The 'graben rule' can propose the depth of the arrested dyke that has induced the event. It relies on the notion that the depth is half the size of the graben width (Pollard et al., 1983; Mastin and Pollard, 1988; Rubin, 1992; Al Shehri and Gudmundsson, 2018). Based on this rule, we can hypothesise that if the dykes that formed the grabens have been arrested, the dyke tips in our study were at 200 m depth for the western graben and at 25 m depth for the eastern graben.

While a dyke propagates towards the surface, the stresses are concentrated and rise at the dyke tips, so fractures are unlikely in their vicinity (Geshi et al., 2010; Philipp et al., 2013). The thickness of the propagating dyke is affected by the overpressure, the dyke strike and the Young's modulus of the crust (stiff layers encourage thin dykes, while soft layers encourage thicker dykes to form); thus, the volcanotectonic studies are mainly schematic (Gudmundsson, 2020).

5.3 Geological reconstruction of the 1928 fissure eruption - a field and numerical synthesis

Our combined study attempted to interpret the possible scenarios that generated the current surficial deformation along the 1928 fissure eruption. In a second step we also attempted to conceptualise the possible scenarios that could have resulted in the formation of the western and eastern grabens studied here, as shown in Figure 14.

Western graben

According to our numerical study, a dyke-induced graben can also be accompanied by a fissure eruption. The field studies (Tibaldi et al., 2022) are unable to define whether the eruptive vents are synchronous with the graben formation during the 1928 event, or a smaller graben was pre-existing to the dyke injection. Our numerical results, however, propose two distinct solutions: A) In low overpressure conditions, dyke arrest is highly possible. The dyke could have induced the graben but not the craters, so the latter could belong to previous eruptions. However, since we know that the vents formed during the 1928 event, we have to disregard this hypothesis. B) In high overpressure conditions, dyke propagation is promoted; hence, a fissure eruption could have followed up the dyke-induced graben. This seems to match the field data, since the eruptive craters are not affected by the graben faults (thus craters postdate faults).

Eastern graben

In this part of the fissure, the dyke has possibly induced a semigraben and a normal graben structure, but no eruption signs are reported; hence, the dyke (and, based on our numerical study, the inclined sheet) should have been arrested at shallow depths. Taking into account the width of these structures, 74 m for the semigraben and 68 m for the graben, according to the 'graben rule' the tip of the dyke should have been arrested at half of this length; approximately 37 m below the semigraben surface and 34 m below the graben surface. However, dykes that come very close to the surface, most of the times, feed eruptions and do not stall (Gudmundsson, 2003; Drymoni, 2020; Drymoni et al., 2020) and narrow grabens imply dykes that are shallow and close to feed an eruption (Hjartardóttir et al., 2016; Trippanera et al., 2014). Instead, our field observations are challenging the following ideas; either that the dykes that propagate very close to the surface usually erupt, or that the 'graben rule' cannot always estimate the tip of the arrested dyke. The efficiency of the 'graben rule' has been already debated by previous studies (Magee and Jackson, 2021) since the fault geometry and the 3D kinematics of the faults play a substantial role in controlling the dyke path. Also, the rate of spreading can affect the eruption scenario (Curewitz and Karson, 1998; Carbotte et al., 2006).

Our hypothesis is that the uprising of a high overpressure inclined sheet and a vertical sheet, respectively, most likely triggered the formation of a semigraben and of a graben. Still, the inclined sheet and the dyke, although reached very shallow levels, they quite likely became arrested (87.5%). This is supported by the sensitivity analysis (Table 1). The process may have been favoured by gravitation instability due to the vicinity of the high scarps of the Ripe della Naca faults.

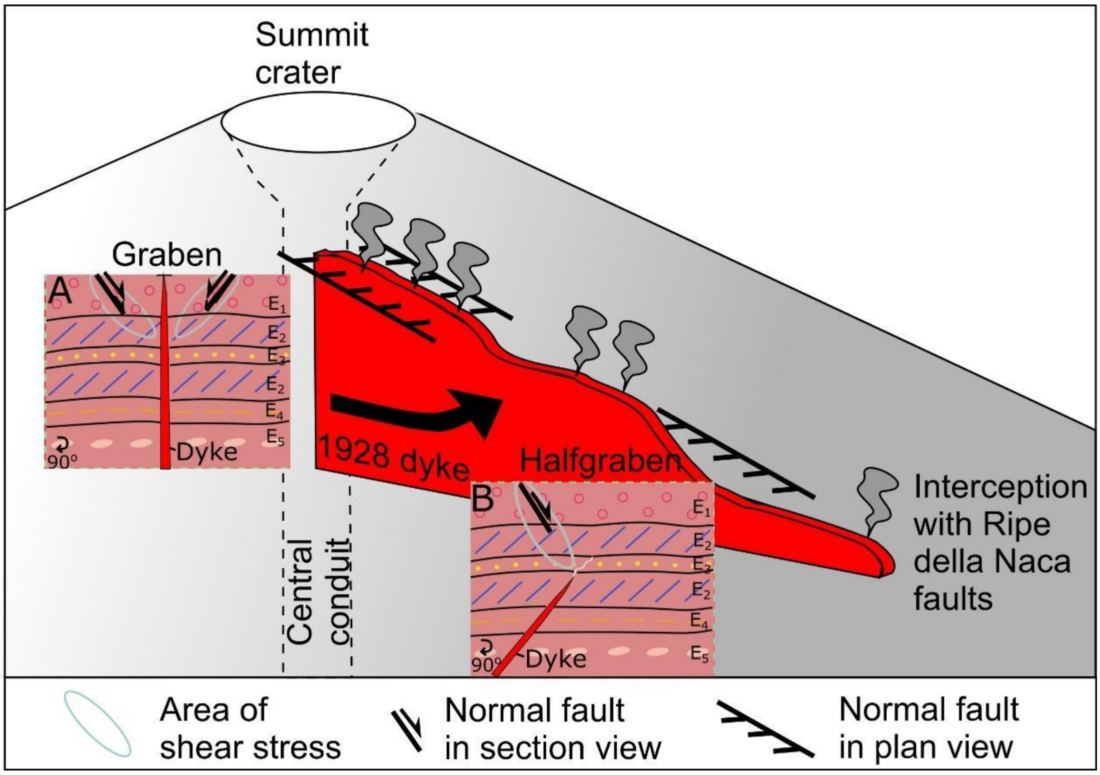

Figure 14. *Schematic illustration of the 1928 dyke on Etna volcano showing the vertical and lateral propagation of the dyke and the surficial deformation as recorded from numerical modelling concepts and structural analyses by Tibaldi et al. (2022). According to our numerical study, the image shows the parameters that could have controlled the propagation of the dyke. A: The dyke induced a graben and a fissure at the surface. B: An inclined finger of the dyke induced a semigraben (or halfgraben) and a graben towards the east without making it to the surface to feed a fissure eruption.*

This is because a stress barrier could have occurred in the stratigraphic sequence and the extensional stress field.

6. Conclusions

Our joint field and numerical modelling analyses suggest the following conclusions to be drawn based on our initial research questions on the propagation of the 1928 dyke on Etna volcano, most of which can have a more general significance:

(i) Regarding the stress barrier conditions:

1. Dyke arrest at the contact with either stiff or soft layers depending to different mechanical conditions. Thick scoria can form temporary stress barriers even if it is at the top or the bottom of the stratigraphic succession. Still, a thin scoria layer (up to 0.1 m) can form temporary stress barriers if they are at the top of the succession. Dyke arrest can also often occur at low mechanical contrast contacts (r = 0.1-0.5).
2. Inclined sheet propagation generates asymmetric tensile and shear stress concentration and dyke arrest concepts.
3. High values of overpressure can raise the stress rotation in a layer but cannot make it sufficient to become a stress barrier (90° stress rotations).
4. The local extensional stress field can promote stress barriers in the soft layers (low F_{ext} values ≤ 2 MPa).

(ii) Regarding the tensile/shear stress concentration and dyke-induced graben concepts:

1) The tensile and shear stress concentration at the dyke tip in a heterogeneous succession is proportional to the overpressure increase.
2) Thick scoria layers suppress the tensile and shear stress concentration if they are at the top of the succession. Still, thin ones at the top or bottom of the stratigraphic column can revoke this condition, and low shear stress concentration can be distributed higher at the succession.
3) At the lowest mechanical contrast contacts and low overpressure (P_o = 1 MPa), shear stress is significantly suppressed compared to other contacts.
4) Stiff layers can build up the shear stress concentration and form narrower grabens, while soft layers tend to disperse them and create wider ones.

5) High overpressure values (P_o = 10 MPa) form narrower grabens while moderate values (P_o = 5 MPa) form wider grabens.
6) If the dyke has managed to propagate to higher levels in the succession, then a narrow graben can form instead of a wide graben.
7) With moderate overpressure values (P_o = 5 MPa), shear stress is concentrated at the stiffer materials, while the soft ones distribute them to higher levels.
8) A dyke-induced graben can be formed if the mechanical contrast (r) is 0.3-2 and the overpressure (P_o) is 5-10 MPa.
9) Soft layers are needed in a heterogeneous succession for dyke-induced graben formation concepts because they concentrate low shear stress values. Still, they distribute it higher towards the surface, while stiff lavas concentrate a high shear stress value and disperse their distribution laterally.
10) The tensile and shear stresses peak at the surface and progressively build up while the dyke moves towards the surface. Still the contact that is ahead of the dyke tip has always the highest stress values during propagation.
11) The layering, the thickness of the layers, their stiffness and local extension can control the wide or narrow structure of a graben.

(iii) Regarding the mechanical and geological evolution of the 1928 fissure:

1) In the western part of the 1928 fracture zone, the dyke-induced graben developed, followed by the further ascent of the dyke that finally intercepted the surface.

2) In the eastern part, an inclined sheet and a vertical dyke triggered the formation of the semigraben and the graben, respectively, and then halted at shallow depth; here, the structure formation process may have been favoured by gravity forces linked to local topography.

Acknowledgments

We thank the editor D. Roman, A. Gudmundsson and an anonymous reviewer for the helpful comments and suggestions. This work was carried out under the aegis of Task Force II of the International Lithosphere Program (Leader A. Tibaldi). K. Drymoni acknowledges a 2-years research fellowship of the Italian Ministry of University and

Research in the framework of a Progetto di Eccellenza grant of the Department of Earth and Environmental Sciences of the University of Milan-Bicocca.

References

Abdelmalak, M.M., Mourgues, R., Galland, O., Bureau, D., 2012. Fracture mode analysis and related surface deformation during dyke intrusion: results from 2D experimental modelling. Earth Planet. Sci. Lett. 359–360, 93–105.

Acocella, V., 2021. Volcano-tectonic processes, Advances in Volcanology, Springer Nature, Switzerland.

Acocella, V., Neri, M., 2009. Dike propagation in volcanic edifices: overview and possible developments, Special Issue: Gudmundsson – Volcanoes, Tectonophysics, 471, 67-77, doi: 10.1016/j.tecto.2008.10.002.

Acocella, V., Trippanera, D., 2016. How diking affects the tectonomagmatic evolution of slow spreading plate boundaries: Overview and model. Geosphere, 12(3), 867-883.

Ágústsdóttir, T., Woods, J., Greenfield, T., Green, R. G., White, R. S., Winder, T., Brandsdóttir B., Steinthórsson S., and Soosalu, H. 2016. Strike-slip faulting during the 2014 Bárðarbunga-Holuhraun dike intrusion, central Iceland. Geophysical Research Letters, 43, 1495–1503. https://doi.org/10.1002/2015GL067423

Al Shehri, A., & Gudmundsson, A., 2018. Modelling of surface stresses and fracturing during dyke emplacement: Application to the 2009 episode at Harrat Lunayyir, Saudi Arabia. Journal of Volcanology and Geothermal Research, 356, 278-303.

Amadei, B., Stephansson, O., 1997. Rock Stress and its Measurement. Chapman and Hall, London.

Azzaro, R., Branca, S., Gwinner, K., Coltelli, M., 2012. The volcano-tectonic map of Etna volcano, 1: 100.000 scale: an integrated approach based on a morphotectonic analysis from high-resolution DEM constrained by geologic, active faulting and seismotectonic data. Italian journal of geosciences, 131(1), 153-170.

Babiker, M., Gudmundsson, A., 2004. The effects of dykes and faults on groundwater flow in an arid land: the Red Sea Hills, Sudan. Journal of Hydrology, 297(1-4), 256-273.

Backers T., Stephansson O., 2012. ISRM Suggested Method for the Determination of Mode II Fracture Toughness. Rock Mech Rock Eng (2012) 45:1011–1022 DOI 10.1007/s00603-012-0271-9

Barabási, A.L., Albert, R., 1999. Emergence of scaling in random networks. Science 286(5439), 509–512.

Bazargan, M., Gudmundsson, A. 2019. Dike-induced stresses and displacements in layered volcanic zones. Journal of Volcanology and Geothermal Research, 384, 189-205.

Becerril, L., Galindo, I., Gudmundsson, A., Morales, J.M., 2013. Depth of origin of magma in eruptions. Sci. Rep. 3, 2762. https://doi.org/10.1038/srep02762.

Bell, F.G., 2000. Engineering Properties of Soils and Rocks, 4th ed., Blackwell Oxford, UK.

Biggs, J., Amelung, F., Gourmelen, N., Dixon, T.H., Kim, S.W., 2009. InSAR observations of 2007 Tanzania rifting episode reveal mixed fault and dyke extension in an immature continental rift, Geophys. J. Int., 179, 549–558.

Biggs, J., Chivers, M., Hutchinson, M.C., 2013. Surface deformation and stress interactions during the 2007–2010 sequence of earthquake, dyke intrusion and eruption in northern Tanzania. Geophysical Journal International, 195(1), 16-26.

Bonafede, M., Danesi, S., 1997. Near-field modifications of stress induced by dyke injection at shallow depth. Geophysical Journal International, 130(2), 435-448.

Bonafede, M., Rivalta, E., 1999. The tensile dislocation problem in a layered elastic medium. Geophysical Journal International, 136(2), 341-356.

Bonforte, A., Gambino, S., Guglielmino, F., Obrizzo, F., Palano, M., Puglisi, G., 2007. Ground deformation modeling of flank dynamics prior to the 2002 eruption of Mt. Etna. Bulletin of Volcanology, 69(7), 757-768.

Borgia, A., Ferrari, L., Pasquarè, G., 1992. Importance of gravitational spreading in the tectonic and volcanic evolution of Mount Etna. Nature 357, 231-235.

Branca, S., Coltelli, M., Groppelli, G., Lentini, F., 2011a. Geological map of Etna volcano, 1: 50,000 scale. Italian Journal of Geosciences, 130(3), 265-291.

Branca, S., Coltelli, M., Groppelli, G., 2011b. Geological evolution of a complex basaltic stratovolcano: Mount Etna, Italy. Italian Journal of Geosciences, 130(3), 306-317.

Branca, S., De Beni, E., Chester, D., Duncan, A., Lotteri, A., 2017. The 1928 eruption of Mount Etna (Italy): Reconstructing lava flow evolution and the destruction and recovery of the town of Mascali. Journal of Volcanology and Geothermal Research, 335, 54-70.

Broek, D., 1982. Elementary engineering fracture mechanics. Springer Science & Business Media.

Browning, J., Gudmundsson, A., 2015. Caldera faults capture and deflect inclined sheets: An alternative mechanism of ring dike formation. Bulletin of Volcanology, 77(1), 4. https://doi.org/10.1007/s00445-014-0889-4

Browning, J., Karaoğlu, Ö., Bayer, Ö., Turgay, M.B., Acocella, V., 2021. Stress fields around magma chambers influenced by elastic thermo-mechanical deformation: implications for forecasting chamber failure. Bulletin of Volcanology, 83(7), 1-13.

Buck, W.R., Einarsson, P., Brandsdóttir, B., 2006. Tectonic stress and magma chamber size as controls on dike propagation: Constraints from the 1975–1984 Krafla rifting episode, J. Geophys. Res., 111, B12404, doi:10.1029/2005JB003879

Cappello, A., Neri, M., Acocella, V., Gallo, G., Vicari, A., Del Negro, C., 2012. Spatial vent opening probability map of Etna volcano (Sicily, Italy). Bulletin of Volcanology, 74(9), 2083-2094.

Carbotte, S.M., Detrick, R.S., Harding, A., Canales, J.P., Babcock, J., Kent, G., Van Ark, E., Nedimovic, M., and Diebold, J., 2006. Rift topography linked to magmatism at the intermediate spreading Juan de Fuca Ridge: Geology, 34, 209–212, https://doi.org/10.1130/G21969.1.

Chadwick, W.W., Embley, R.W., 1998. Graben formation associated with recent dike intrusions and volcanic eruptions on the mid-ocean ridge: Journal of Geophysical Research, 103, 9807–9825.

Clunes, M., Browning, J., Cembrano, J., Marquardt, C., Gudmundsson, A., 2021. Crustal folds alter local stress fields as demonstrated by magma sheet—Fold interactions in the Central Andes. Earth and Planetary Science Letters, 570, 117080.

Cocina, O., Neri, G., Privitera, E., Spampinato, S., 1997. Stress tensor computations in the Mount Etna area (Southern Italy) and tectonic implications. J. Geodyn. 23(2), 109-127.

Cocina, O., Neri, G., Privitera, E., Spampinato, S., 1998. Seismogenic stress field beneath Mt. Etna (South Italy) and possible relationships with volcano-tectonic features. J. Volcanol. Geoth. Res., 83, (3), 335-348.

Curewitz, D., Karson, J.A., 1998. Geological consequences of dike intrusion at mid-ocean ridge spreading centers: in Buck, W.R., et al, eds., Faulting and magmatism at mid-ocean ridges: American Geophysical Union Geophysical Monograph 106 , 117–136.

Dahm, T., 1996. Elastostatic simulation of dislocation sources in heterogeneous stress fields and multilayered media having irregular interfaces, Phys. Chem. Earth, 21, 241-246.

Dahm, T., 2000. Numerical simulations of the propagation path and the arrest of fluid-filled fractures in the Earth, Geophysical Journal International, 141, (3), 623–638,

Deb, D., 2006. Finite Element Method: Concepts and Applications in Geomechanics. Prentice-Hall, New Jersey.

Delaney, P.T., Pollard, D.D., Ziony, J.I. McKee, E.H., 1986. Field relations between dikes and joints: Emplacement processes and paleostress analysis, J. Geophys. Res., 91, 4920-4938.

Delaney, J.R., Kelley, D.S., Lilley, M.D., Butterfield, D.A., Baross, J.A., Wilcock, W.S. et al., 1998. The quantum event of oceanic crustal accretion: Impacts of diking at mid-ocean ridges. Science, 281(5374), 222-230.

Dieterich, J.H., Decker, R.W., 1975. Finite Element Modelling of Surface Deformation Associated with Volcanism. J. Geophys. Res., 80, p. 4094-4102.

Drymoni, K., 2020. Dyke propagations paths: The movement of magma from the source to the surface, PhD thesis, Royal Holloway University of London, UK

Drymoni, K., Browning, J., Gudmundsson, A., 2020. Dyke-arrest scenarios in extensional regimes: Insights from field observations and numerical models, Santorini, Greece. Journal of Volcanology and Geothermal Research, 396, 106854.

Drymoni, K., Browning, J., Gudmundsson, A., 2021. Volcanotectonic interactions between inclined sheets, dykes, and faults at the Santorini Volcano, Greece. Journal of Volcanology and Geothermal Research, 107294.

Drymoni, K., Browning, J., Gudmundsson, A., 2022. Spatial and temporal volcanotectonic evolution of Santorini volcano, Greece. Bulletin of Volcanology, 84(6), 1-18.

Dumont, S., Klinger, Y., Socquet, A., Doubre, C., Jacques, E., 2017. Magma influence on propagation of normal faults: Evidence from cumulative slip profiles along Dabbahu-Manda-Hararo rift segment (Afar, Ethiopia): Journal of Structural Geology, 95,48–59 https://doi.org/10.1016/j.jsg.2016.12.008.

Ebinger, C., Ayele, A., Keir, D., Rowland, J., Yirgu, G., Wright, T., Belachew, M., Hamling I., 2010. Length and timescales of rift faulting and magma intrusion: The Afar rifting cycle from 2005 to present, Annu. Rev. Earth Planet. Sci., 38, 439–466.

Feuillet, N. (2013). The 2011–2012 unrest at Santorini rift: stress interaction between active faulting and volcanism. Geophysical Research Letters, 40(14), 3532-3537.

Gambino, S., Barreca, G., Bruno, V., De Guidi, G., Ferlito, C., Gross, F., et al., 2022. Transtension at the Northern Termination of the Alfeo-Etna Fault System (Western Ionian Sea, Italy): Seismotectonic Implications and Relation with Mt. Etna Volcanism. Geosciences, 12(3), 128.

Geyer, A., Gottsmann, J., 2010. The influence of mechanical stiffness on caldera deformation and implications for the 1971–1984 Rabaul uplift (Papua New Guinea). Tectonophysics, 483(3-4), 399-412.

Geshi, N., Kusumoto, S., Gudmundsson, A., 2010. Geometric difference between non-feeder and feeder dikes. Geology, 38(3), 195-198.

Geshi, N., Neri, M., 2014. Dynamic feeder dyke systems in basaltic volcanoes: the exceptional example of the 1809 Etna eruption (Italy). Frontiers in Earth Science, 2, 13.

Giampiccolo, E., Cocina, O., De Gori, P., Chiarabba, C., 2020. Dyke intrusion and stress-induced collapse of volcano flanks: the example of the 2018 event at Mt. Etna (Sicily, Italy). Scientific reports, 10(1), 1-8.

Grandin, R.E., Jacques, A., Nercessian, A., Ayele, C., Doubre, et al. 2011. Seismicity during lateral dike propagation: Insights from new data in the recent Manda Hararo-Dabbahu rifting episode (Afar, Ethiopia). Geochemistry, Geophysics, Geosystems, AGU and the Geochemical Society, 12 (4) doi:10.1029/2010GC003434

Greenland, L.P., Rose, W.I., Stokes, J.B., 1985. An estimate of gas emissions and magmatic gas content from Kilauea volcano. Geochim. Cosmochim. Acta 49, 125–129.

Groppelli, G., Tibaldi, A., 1999. Control of rock rheology on deformation style and slip-rate along the active Pernicana Fault, Mt. Etna, Italy. Tectonophysics, 305(4), 521-537.

Gudmundsson, A., 1984.Tectonic aspects of dykes in northwestern Iceland. Jökull (Iceland Journal of Earth Sciences) 34, 81-96.

Gudmundsson, A., 1984. Formation of dykes, feeder-dykes, and the intrusion of dykes from magma chambers. Bulletin Volcanologique, 47, 537-550.

Gudmundsson, A., 1987. Lateral magma flow, caldera collapse, and a mechanism of large eruptions in Iceland. Journal of Volcanology and Geothermal Research, 34, 65-78.

Gudmundsson, A., 2003. Surface stresses associated with arrested dykes in rift zones: Bulletin of Volcanology, 65, 606–619, https://doi.org/10.1007/s00445-003-0289-7.

Gudmundsson, A., 2007. Infrastructure and evolution of ocean-ridge discontinuities in Iceland. Journal of Geodynamics, 43(1), 6-29.

Gudmundsson, A., 2011. Rock fractures in geological processes. Cambridge University Press.

Gudmundsson, A., 2012. Magma chambers: Formation, local stresses, excess pressures, and compartments. J Volcanol Geotherm Res 237, 19–41.

Gudmundsson, A., 2020. Volcanotectonics: Understanding the structure, deformation and dynamics of volcanoes. Cambridge University Press.

Gudmundsson, A., 2022. The propagation paths of fluid-driven fractures in layered and faulted rocks. Geological Magazine, 1-24.

Haimson, B.C., Rummel, F., 1982. Hydrofracturing stress measurements in the Iceland research drilling project drill hole at Reydarfjördur, Iceland. J. Geophys. Res., 87, 6631–6649.

Heap, M.J., Villeneuve, M., Albino, F., Farquharson, J.I., Brothelande, E., Amelung, F., Got, J.L., Baud, P., 2020. Towards more realistic values of elastic moduli for volcano modelling. Journal of volcanology and geothermal research, 390, 106684.

Heimisson, E. R., Hooper, A., & Sigmundsson, F. 2015. Forecasting the path of a laterally propagating dike. Journal of Geophysical Research: Solid Earth, 120(12), 8774-8792.

Hjartardóttir, Á.R., Einarsson, P., Gudmundsson, M.T., Högnadóttir, T., 2016. Fracture movements and graben subsidence during the 2014 Bárðarbunga dike intrusion in Iceland: Journal of Volcanology and Geothermal Research, 310, 242–252, https://doi.org/10.1016/j.jvolgeores.2015.12.002.

Holland, M., van Gent, H.W., Bazalgette, L., Yassir, N., Hoogerduijn Strating, E.H., Urai, J.L., 2011. Evolution of dilatant fracture networks in a normal fault — evidence from 4D model experiments Earth Planet Sci. Lett., 304, 399-406

Hooper, A., B. Ófeigsson, F. Sigmundsson, B. Lund, P. Einarsson, H. Geirsson, and E. Sturkell (2011), Increased capture of magma in the crust promoted by ice-cap retreat in Iceland, Nat. Geosci., 4(11), 783–786, doi:10.1038/ngeo1269.

Kanamori, H., Anderson, D.L., 1975. Theoretical basis of some empirical relations in seismology. Bull. Seismol. Soc. Am. 65, 1074–1095

Kavanagh, J., Menand, T., Sparks, R., 2006. An experimental investigation of sill formation and propagation in layered elastic media. Earth Planet. Sci. Lett. 245, 799–813.

Kieffer, G., 1983. L'évolution structurale de l'Etna (Sicile) et les modalités du contrôle tectonique et volcano tectonique de son activité. Faits et hypothèses après les éruptions de 1978 et 1979. Revue de Géologie Dynamique et de Géographie physique, 24, Fasc. 2, p. 129-152.

Kieffer, G., 1985. Évolution structurale et Dynamique d'un Grand Vulcan Polygénique: stades d'Éducation et Activité actuelle de l'Etna (Sicile). Thesis, Université Clermont-Ferrand, 497

Koehn, D., Steiner, A., and Aanyu, K. 2019, Modelling of extension and dyking-induced collapse faults and fissures in rifts: Journal of Structural Geology, 118, 21–31, https://doi.org/10.1016/j.jsg.2018.09.017.

Kolzenburg, S., Kubanek, J., Dirscherl, M., Hamilton, C.W., Hauber, E., Scheidt, S. P., Münzer, U., 2022. Solid as a rock: Tectonic control of graben extension and dike propagation. Geology, 50(3), 260-265.

Lanzafame, G., Neri, M., Coltelli, M., Lodato, L., Rust, D., 1997. North-South compression in the Nit. Etna region (Sicily): spatial and temporal distribution. Acta Vulcanol. 9, 121-134.

Maccaferri, F., Bonafede, M., Rivalta, E., 2011. A quantitative study of the mechanisms governing dike propagation, dike arrest and sill formation, J. Volcanol. Geotherm. Res., 208, 39–50

Maccaferri, F., Rivalta, E., Passarelli, L., Aoki, Y., 2016. On the mechanisms governing dike arrest: Insight from the 2000 Miyakejima dike injection, Earth Planet. Sci. Lett., 434, 64–74.

Magee, C., Jackson, C.A.-L., 2021. Can we relate the surface expression of dike-induced normal faults to subsurface dike geometry? Geology, 49, https://doi.org/10.1130/G48171.1

Manighetti I., King, G. Sammis, C.G., 2004. The role of off-fault damage in the evolution of normal faults. Earth Planet. Sci. Lett., 217 (3), 399-408.

Masterlark, T., Tung, S., 2018. Finite Element Models of Elastic Volcano Deformation. Volcanoes-Geological and Geophysical Setting, Theoretical Aspects and Numerical Modeling, Applications to Industry and Their Impact on the Human Health.

Mastin, L.G., Pollard, D.D., 1988. Surface deformation and shallow dike intrusion processes at Inyo Craters, Long Valley, California, J. Geophys. Res., 93, 13,221–13,235, doi:10.1029/JB093iB11p13221.

McGuire, W.J., Pullen, A.D., 1989. Location and orientation of eruptive fissures and feeder dykes at Mount Etna; influence of gravitational and regional tectonic stress regimes. Journal of Volcanology and Geothermal Research, 38(3-4), 325-344.

McGuire, W.J., Saunders, S.J., 1993. Recent earth movements at active volcanoes: a review. Quat. Proc. 3, 33-46.

Mériaux, C., Lister, J.R. 2002. Calculation of dike trajectories from volcanic centers, J. Geophys. Res., 107(B4), 2077

Murray, J. B., & Pullen, A.D., 1984. Three-dimensional model of the feeder conduit of the 1983 eruption of Mt. Etna volcano, from ground deformation measurements. Bulletin Volcanologique, 47(4), 1145-1163.

Neri, M., Garduno, V.H., Pasquarè, G., Rasà, R., 1991. Studio strutturale e modello cinematico della valle del Bove e del settore nord-orientale etneo. Acta Vulcanol. 1, 17-24.

Neri, M., Acocella, V., Behncke, B., Giammanco, S., Mazzarini, F., Rust, D., 2011. Structural analysis of the eruptive fissures at Mount Etna (Italy). Annals of Geophysics, 54, 464-479.

Okada, Y., 1985. Surface deformation due to shear and tensile faults in a half-space. Bulletin of the seismological society of America, 75(4), 1135-1154.

Opheim, J.A. Gudmundsson, A., 1989. Formation and geometry of fractures and related volcanism of the Krafla fissure swarm, Northeast Iceland Geol. Soc. Am. Bull., 101, 1608-1622

Palano, M., 2016. Episodic slow slip events and seaward flank motion at Mt. Etna volcano (Italy). Journal of Volcanology and Geothermal Research, 324, 8-14.

Palano, M., Gresta, S., Puglisi, G., 2009. Time-dependent deformation of the eastern flank of Mt. Etna: after-slip or viscoelastic relaxation? Tectonophysics, 473(3-4), 300-311.

Pallister, J. S., et al., 2010. Broad accommodation of rift-related extension recorder by dyke intrusion in Saudi Arabia, Nat. Geosci., 3(10), 708–712, doi:10.1038/ngeo966.

Passarelli, L., Maccaferri, F., Rivalta, E., Dahm, T., Abebe Boku, E., 2012. A probabilistic approach for the classification of earthquakes as “triggered” or “not triggered”, J. Seismol., 17, 165–187.

Philipp, S.L., Afşar, F., Gudmundsson, A., 2013. Effects of mechanical layering on hydrofracture emplacement and fluid transport in reservoirs. Frontiers in Earth Science, 1, 4.

Pollard, D.D., Delaney, P.T., Duffield, W.A., Endo, E.T., Okamura, A.T., 1983. Surface deformation in volcanic rift zones. Tectonophysics 94, 541–584.

Pollard, D.D., Holzhausen, G. 1979. On the mechanical interaction between a fluid-filled fracture and the earth's surface Tectonophysics, 53, 27-57.

Reddy, J.N. 2013. An Introduction to Continuum Mechanics, Cambridge Univ. Press, New York

Rivalta, E., Dahm, T., 2004. Dyke emplacement in fractured media: Application to the 2000 intrusion at Izu islands, Japan, Geophys. J. Int., 157, 283–292.

Rivalta, E., Corbi, F., Passarelli, L., Acocella, V., Davis, T., Di Vito, M.A., 2019. Stress inversions to forecast magma pathways and eruptive vent location. Science advances, 5(7), eaau9784.

Roman, D.C., Cashman, K.V., (2006). The origin of volcano-tectonic earthquake swarms. Geology, 34(6), 457-460.

Roman, D.C., Neuberg, J., Luckett, R.R. (2006). Assessing the likelihood of volcanic eruption through analysis of volcanotectonic earthquake fault–plane solutions. Earth and Planetary Science Letters, 248(1-2), 244-252.

Rowland, J.V., Baker, E., Ebinger, C.J., Keir, D., Kidane, T., Biggs, J., Wright, T.J. 2007. Fault growth at a nascent slow-spreading ridge: 2005 Dabbahu rifting episode, Afar, Geophys. J. Int., 171(3), 1226–1246, doi:10.1111/j.1365-246X.2007.03584.x.

Rubin, A.M., 1992. Dike-induced faulting and graben subsidence in volcanic rift zones. Journal of Geophysical Research: Solid Earth, 97(B2), 1839-1858.

Rubin, A.M. 1993. Tensile fracture of rock at high confining pressure: Implications for dike propagation. Journal of Geophysical Research, 98(B9), 15,919–15,935.

Rubin, A.M., Pollard, D.D., 1988. Dike-induced faulting in rift zones of Iceland and Afar, Geology, 16, 413–417.

Ruch, J., Wang, T., Xu, W., Hensch, M., Jónsson, S., 2016. Oblique rift opening revealed by reoccurring magma injection in central Iceland: Nature Communications, 7, 12352, https://doi.org/10.1038/ncomms12352.

Ruz, J., Browning, J., Cembrano, J., Iturrieta, P., Gerbault, M., Sielfeld, G., 2020. Field observations and numerical models of a Pleistocene-Holocene feeder dyke swarm associated with a fissure complex to the east of the Tatara-San Pedro-Pellado complex, Southern Volcanic Zone, Chile. Journal of Volcanology and Geothermal Research, 404, 107033.

Schultz, R.A., 1995. Limits on strength and deformation properties of jointed basaltic rock masses. Rock Mech. Rock Eng., 28, 1–15.

Scudero, S., De Guidi, G., Gudmundsson, A., 2019. Size distributions of fractures, dykes, and eruptions on Etna, Italy: Implications for magma-chamber volume and eruption potential. Sci. Re 9, 4139

Segall, P., Cervelli, P., Owen, S., Lisowski, M., & Miklius, A. (2001). Constraints on dike propagation from continuous GPS measurements. Journal of Geophysical Research: Solid Earth, 106(B9), 19301-19317.

Sigurdsson, O., 1980. Surface deformation of the Krafla fissure swarm in two rifting events, J. Geophys., 47, 154–159.

Tanguy, JC., 1981. Les éruptions historiques de l'Etna: chronologie et localisation. Bull. Volcanol., 44, 585-640.

Tibaldi, A., 2015. Structure of volcano plumbing systems: a review of multi-parametric effects. J. Volcanol. Geotherm. Res., 298, 85–135.

Tibaldi, A., Groppelli, G., 2002. Volcano-tectonic activity along structures of the unstable NE flank of Mt. Etna (Italy) and their possible origin J. Volcanol. Geotherm. Res., 115 (2002), 277-302.

Tibaldi, A., Bonali, F.L., Russo, E., Fallati, L., 2020. Surface deformation and strike-slip faulting controlled by dyking and host rock lithology: A compendium from the Krafla Rift, Iceland. Journal of Volcanology and Geothermal Research, 395, 106835.

Tibaldi, A., Bonali, F.L., Corti, N., Russo, E., Drymoni, K., De Beni, E., Branca, S., Neri, M., Cantarero, M., Pasquarè Mariotto, F., 2022. Surface deformation during the 1928 fissure eruption of Mt. Etna (Italy): Insights from field data and FEM numerical modelling. Tectonophysics, in press.

Trippanera, D., Acocella, V., Ruch, J., 2014. Dike-induced contraction along oceanic and continental divergent plate boundaries. Geophysical Research Letters, 41(20), 7098-7104.

Trippanera, D., Ruch, J., Passone, L., Jónsson, S., 2019. Structural mapping of dike-induced faulting in Harrat Lunayyir (Saudi Arabia) by using high resolution drone imagery. Frontiers in Earth Science, 7, 168.

Villani, F., Pucci, S., Azzaro, R., Civico, R., Cinti, F. R., Pizzimenti, L., G. Tarabusi, S. Branca, C.A. Brunori, M. Caciagli, M. Cantarero, Cucci, L., D’Amico S., De Beni, E., De Martini, P.M., Mariucci, M.T., Messina, A., Montone, P., Nappi R., Nave, R., Pantosti, D., Ricci, T., Sapia, V., Smedile, A., Vallone, R., Venuti, A., 2020. Surface ruptures database related to the 26 December 2018, MW 4.9 Mt. Etna earthquake, southern Italy. Scientific data, 7(1), 1-9.

von Hagke, C., Kettermann, M., Bitsch, N., Bücken, D., Weismüller, C., Urai, J.L., 2019. The effect of obliquity of slip in normal faults on distribution of open fractures: Frontiers in Earth Science, 7, 18, https://doi.org/10.3389/feart.2019.00018.

Xu, W., Jónsson, S., Corbi, F., Rivalta, E., 2016. Graben formation and dike arrest during the 2009 Harrat Lunayyir dike intrusion in Saudi Arabia: Insights from InSAR, stress calculations and analog experiments: Journal of Geophysical Research: Solid Earth, 121, 2837–2851, https://doi.org/10.1002/2015JB012505.